IL-1R signaling drives enteric glia-macrophage interaction in colorectal cancer progression

Lies van Baarle[1,12], Veronica De Simone[1,12], Linda Schneider[2,12], Sneha Santhosh[1,7], Saeed Abdurahiman[1], Francesca Biscu[1,8], Reiner Schneider[2], Lisa Zanoletti[1,9], Sara Verbandt[3], Zedong Hu[3], Michelle Stakenborg[1], Bo-Jun Ke[1], Balbina García-Reyes[2,10], Jonas Henn[2], Marieta Toma[4], Maxime Vanmechelen[5,11], Frederik De Smet[5,11], Sales Ibiza[6], Sabine Tejpar[3], Sven Wehner[2,13,*] and Gianluca Matteoli[1, 11, 13,14,*]

[1]Department of Chronic Diseases, Metabolism and Ageing (CHROMETA), Translational Research Center for Gastrointestinal Disorders (TARGID), KU Leuven, Leuven, Belgium

[2]Department of Surgery, University Hospital Bonn, Medical Faculty, Bonn, Germany

[3]Digestive Oncology, Department of Oncology, KU Leuven, Leuven, Belgium

[4]Department of Pathology, University Hospital Bonn, Medical Faculty, Bonn, Germany

[5]Laboratory for Precision Cancer Medicine, Translational Cell and Tissue Research Unit, Department of Imaging & Pathology, KU Leuven, Leuven, Belgium

[6]Laboratory of Cell Biology & Histology, Department of Veterinary Sciences, University of Antwerp, Antwerp, Belgium

[7]Department of Anatomy and Physiology, University of Melbourne, Parkville, VIC, 3010, Australia

[8]Centre for Inflammation Research, University of Edinburgh, Edinburgh, United Kingdom

[9]Department of Biology and Biotechnology "L. Spallanzani", University of Pavia, Pavia, Italy

[10]Mildred Scheel School of Oncology, Aachen Bonn Cologne Düsseldorf (MSSO ABCD), University Hospital Bonn, Medical Faculty, Bonn, Germany

[11]Leuven Institute for Single-cell Omics (LISCO), KU Leuven, Leuven, Belgium

[12]These authors contributed equally

[13]Senior authors

[14]Lead contact

*Correspondence: sven.wehner@ukbonn.de (S.W.), gianluca.matteoli@kuleuven.be (G.M.)

SUMMARY

Enteric glial cells (EGCs) have been recently recognized as key components of the colonic tumor microenvironment (TME) indicating their potential role in colorectal cancer (CRC) pathogenesis. Although EGCs modulate immune responses in other intestinal diseases, their interaction with the CRC immune cell compartment remains unclear. Through a combination of single-cell and bulk RNA-sequencing, both in CRC murine models and patients, we found that EGCs acquire a reactive and immunomodulatory phenotype that drives tumor-associated macrophage (TAM) differentiation. Tumor-infiltrating monocytes direct CRC EGC phenotypic and functional switch via IL-1R signaling pathway. In turn, tumor EGCs promote monocyte differentiation towards pro-tumorigenic $SPP1^+$ TAMs via secretion of IL-6. Finally, the distinct tumor EGC phenotype correlates with worse disease outcome in patients suffering from CRC. Our study reveals a previously unexplored and crucial neuroimmune interaction between EGCs and TAMs in the colorectal TME, providing important insights into CRC pathogenesis.

KEYWORDS: Colorectal Cancer; Enteric glia cells; Tumor Associated Macrophages; tumor microenvironment; neuroimmune crosstalk; IL-1R/IL-6 axis; $SPP1^+$ TAMs; IL-1R signaling

INTRODUCTION

Identified as the world's third most common cancer, colorectal cancer (CRC) represents one of the preeminent causes of cancer-associated deaths worldwide. Although innovative technologies have significantly impacted the diagnosis, surgery, and treatment of CRC, patients with advanced disease still have a very poor prognosis. In fact, while the 5-year survival rates of patients with early-stage CRC can reach up to 90%, the survival rate plummets dramatically to as low as 10% for patients diagnosed with advanced metastasis[1]. This suggests a clear unmet need for more effective therapy for the treatment of these patients.

CRC consists of rapidly evolving neoplasms where acquired mutations in oncogenes and tumor-suppressor genes lead to increasing complexity of the tumor microenvironment (TME), unleashing interaction of the tumor cells with the stroma and the immune system, including fibroblasts, tumor-infiltrating immune cells, and neuronal cells[2,3]. This process contributes to the formation of a complex network of cell types within the TME, which is crucial for tumor survival and fitness.

In recent years, enteric glial cells (EGCs) have also been identified as a constituent of the colon carcinoma microenvironment[4,5]. EGCs, once regarded as merely supportive and accessory cells for neurons within the enteric nervous system[6], have now gained increased attention for their more complex roles in both health and disease[7]. Indeed, accumulating evidence highlights EGCs as crucial mediators of interactions among enteric neurons, intestinal epithelium, enteroendocrine cells, and immune cells[7–10]. Of particular interest is their significant role in modulating immune responses in various intestinal diseases[11–14]. In this regard, we recently demonstrated that EGCs significantly affect macrophage recruitment and differentiation in a murine model of acute intestinal inflammation such as post-operative ileus[15,16].

In the context of CRC, a few studies suggested that EGCs exert a pro-tumorigenic effect during tumor development[4,5]. However, the mechanisms by which EGCs interact with the different components of the colorectal cancer TME to exert their pro-tumorigenic role remain poorly understood. In this study, we demonstrated that upon exposure to the colorectal TME, EGCs undergo a reactive phenotypic switch, leading to the activation of immunomodulatory processes that promote the differentiation of tumor-associated macrophages (TAMs). Intriguingly, tumor-infiltrating monocytes were found to influence the phenotype and function of CRC EGCs through the IL-1 signaling pathway. In turn, EGCs-derived IL-6 promoted the differentiation of these monocytes towards SPP1^{+} TAMs. Importantly, this IL-1R/IL-6 axis was found to be essential for the tumor-supportive functions of EGCs. Collectively, our results reveal a previously unrecognized neuroimmune interaction within the colon cancer microenvironment. Thereby, our findings deepen the understanding of CRC pathogenesis

and could facilitate the development of novel therapeutic strategies for the treatment of this devastating disease.

RESULTS

EGCs shape the CRC immune compartment

Despite recent studies having identified EGCs as an important component of the colon TME, the way they contribute to CRC pathogenesis and their possible interaction with the immune compartment in the tumor remains unexplored. Hence, to address the immunomodulatory role of enteric glia in CRC, we made use of a murine orthotopic CRC model (Figure S1A) in PLP1^{CreERT2}iDTR mice allowing temporal regulation of EGC depletion during colon tumor development. Following tamoxifen exposure, diphtheria toxin (DT) was delivered by colonoscopy-guided injections into the colonic wall on days -5 and -3 (Figure 1A). This resulted in local EGC depletion on day 0, as indicated by decreased GFAP protein level at the injection site (Figures S1B and S1C). Seven days after tumor induction, a significant reduction of tumor formation was observed in DT pre-treated mice compared to the Vehicle group (Figure 1B). Interestingly, in the early phase of tumor expansion, EGC depletion resulted in decreased TAMs, monocytes, and eosinophils, while no difference was observed for neutrophils or T and B cells (Figures 1C, S1D, and S1E). In line, in an orthotopic co-injection model of MC38 cells and primary murine EGCs, tumor growth and TAMs, as well as CD4$^+$ T cell, CD8$^+$ T cell, and T_{reg} cell numbers were significantly increased compared to the mice orthotopically injected with MC38 cells alone (Figures 1D-1F and S1F). Notably, T_{reg} increase might be due to the high number of TAMs observed in this model, as already proven that TAMs induce T_{reg} cell expansion within the TME[17]. Overall, these findings suggest that EGCs participate in shaping the tumor immune microenvironment, mainly by expanding the TAM population.

Using spatial mapping via confocal immunofluorescence, we observed a close interaction between EGCs (GFAP) and TAMs (F4/80) within orthotopic colonic tumors (Figure 1G), further suggesting the existence of this neuroimmune interplay within the TME.

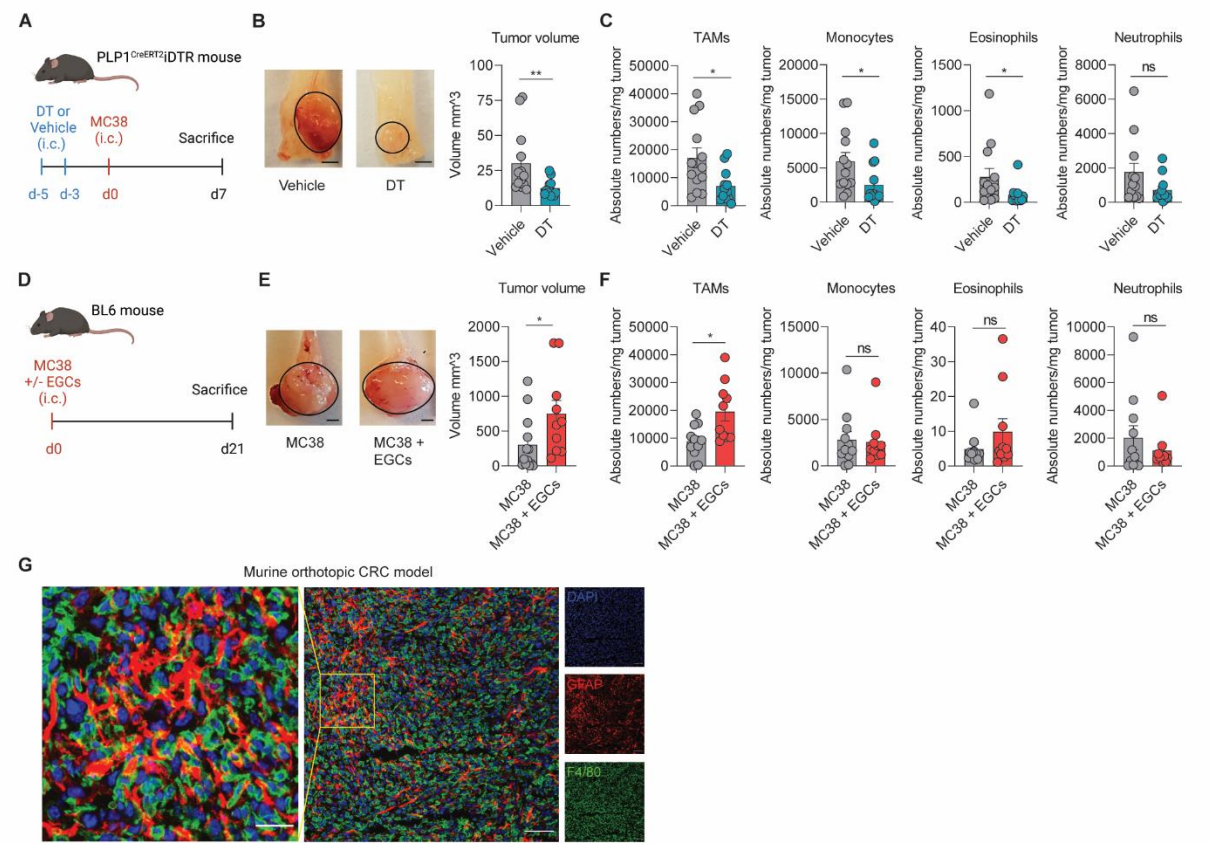

Figure 1. EGCs shape the CRC immune compartment
(A-C) PLP1^{CreERT2}iDTR mice were intracolonically (i.c.) injected at day(d)-5 and d-3 with 40 ng Diphtheria toxin (DT) or saline (Vehicle). At d0, MC38 cells were i.c. injected in both groups. Tumor growth and myeloid immune infiltration were assessed at d7. Schematic representation of EGCs depletion mouse model (A) with representative pictures (scale bar 2 mm) and quantitative comparison of tumor volume (B). Data show absolute tumor-infiltrating myeloid immune cell numbers per mg tumor tissue (C) (*n = 13* Vehicle, *n = 12* DT).
(D-F) BL6 mice were i.c. injected at d0 with MC38 cells with or without embryonic neurosphere-derived EGCs (1:1 ratio). Tumor growth and myeloid immune infiltration were assessed at d21. Schematic representation of EGCs co-injection mouse model (D) with representative pictures (scale bar 2 mm) and quantitative comparison of tumor volume (E). Data show absolute tumor-infiltrating myeloid immune cell numbers per mg tumor tissue (F) (*n = 11* MC38, *n = 10* MC38 + EGCs).
(G) Representative image showing GFAP (red), F4/80 (green) and DAPI (blue) in orthotopic murine tumor sections, (scale bar 70 µm and 25 µm). Data show mean ± SEM. Statistical analysis: unpaired Mann-Whitney test (B-C, E-F) *p < 0.05, **p < 0.005, ns not significant. See also Figure S1.

EGCs display an activated and immunomodulatory phenotype in CRC

To examine the mechanisms by which EGCs affect the immune CRC compartment with particular regard to the TAMs, we first investigated their transcriptional adaptations upon CRC onset. To this end, we established an *in vitro* tumor EGC model able to mimic the response of EGCs to the factors secreted by the colonic TME. These EGCs, from now onwards defined as TME-conditioned medium-treated EGCs (TME-CM EGCs), were generated by stimulating primary EGCs with the CM of digested murine MC38 orthotopic tumor tissues (Figure 2A). Bulk RNA sequencing (RNA-seq) was

performed to determine transcriptional differences in TME-CM EGCs, compared to unstimulated and healthy conditioned medium-treated (H-CM) primary EGCs, at different time points. Principal component analysis (PCA) revealed that H-CM and unstimulated EGCs samples clustered well together with only 66 differentially expressed genes among them. In contrast, a clear separation between TME-CM EGCs compared to H-CM and unstimulated EGCs suggested a distinct phenotype for murine CRC EGCs (Figure 2B). Indeed, we found that TME-CM EGCs differed by 610 genes and 298 genes with H-CM EGCs and unstimulated EGCs, respectively. Subsequently, weighted gene correlation network analysis (WGCNA) revealed 12 identified gene co-expression modules. TME-CM EGCs showed specific correlation to modules 7 and 8 and an inverse correlation to module 4 (Table S1; Figure 2C). Here, module 7 showed a functional association with glial reactivity, indicated by the upregulation of genes such as *Lcn2* and *Timp1*, which are typical markers for pan-reactive astrocytes[18] (Figure 2D). Module 8 included genes associated with immunomodulatory functions of EGCs mimicking an enteric gliosis state, including *Ccl2* and *Il6*[16]. On the contrary, the genes of module 4, such as *Ntsr1* and *Sparlc1,* were associated with the homeostatic functions of EGCs[19]. In line, gene set enrichment analysis of the 24h TME-CM EGCs signature revealed impairment for functions previously ascribed to healthy EGCs, including GO terms like "*Positive regulation of stem cell differentiation", "Regulation of glial cell differentiation and gliogenesis", "Neuron projection guidance"* and *"Positive regulation of neurogenesis"*[7,20] (Figure 2E; Table S2). Notably, in addition to CRC pathogenesis pathways, TME-CM EGCs were enriched for the GO terms "*Positive regulation of prostaglandin biosynthetic process"* and "*Interleukin 1 receptor activity"*, in line with the previous findings of Valès et al., which suggested a paracrine IL-1/PGE_2 signaling for CRC EGCs[4]. Lastly, gene set enrichment analysis predicted a direct interaction of CRC EGCs with TAMs, reflected by functional enrichment for the GO terms "*Macrophage differentiation"* and *"Positive regulation of macrophage activation* and *migration"* (Figure 2E). Taken together, upon exposure to the CRC TME, EGCs undergo a phenotypic switch associated with the activation of immunomodulatory programs related to macrophage interplay.

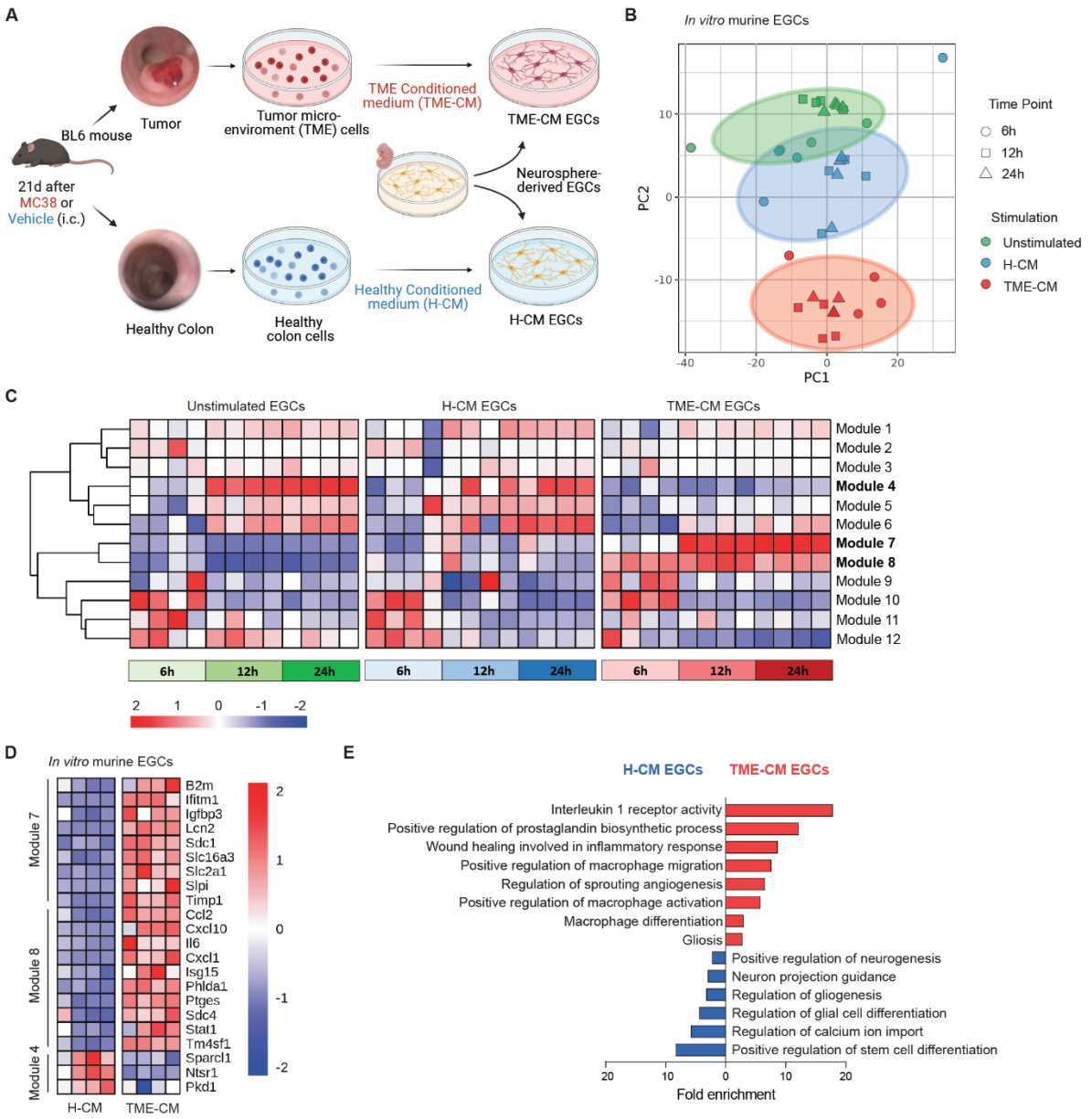

Figure 2. EGCs display an activated and immunomodulatory phenotype in CRC

Transcriptome analysis of *in vitro* primary embryonic neurosphere-derived EGCs alone or stimulated with healthy conditioned medium (H-CM) or tumor microenvironment conditioned medium (TME-CM) at different time points (6h, 12h, and 24h, *n = 4*).

(A) Schematic representation of the *in vitro* tumor EGCs model.

(B) Principal component analysis (PCA) plot of EGCs gene signature identified by 3´mRNA bulk RNA-seq. Each dot represents an individual sample.

(C) Heatmap showing the transcriptional modules identified by weighted gene correlation network analysis (WGCNA).

(D) Heatmap of differentially expressed genes in modules 4, 7, and 8 of *in vitro* murine EGCs stimulated for 24h with H- or TME-CM.

(E) Gene set enrichment analysis for the differentially up- and down-regulated genes in TME-CM versus H-CM stimulated EGCs after 24h (*n = 4*). See also Table S1 and S2.

Tumor EGC-derived IL-6 favors SPP1$^+$ TAM differentiation

The transcriptomic analysis predicted a direct interaction of EGCs with TAMs in the colonic TME. Consequently, we aimed at understanding how EGCs could shape the TAM population within CRC. Firstly, to characterize the immune landscape of colorectal tumors, we analysed a total of 5210 immune cells from mice bearing orthotopic tumors using single cell transcriptomics (Figure S2A). Interestingly, among the identified immune populations, monocytes and macrophages accounted for 60% of the tumor-infiltrating immune cells. Further unsupervised clustering of the myeloid cells (*Lyz2, Cd68, H2-Ab1, Mrc1, C1qa, Ly6c2, Ccr2,* and *Fn1*) revealed 1 monocyte and 4 distinct macrophage populations (Figures 3A and 3B). As the most abundant macrophage cluster was characterized by marker genes for both monocytes (*Ccr2* and *Ly6c2)* and macrophages (*H2-Ab1* and *Nlrp3),* indicating a transitional state, we named this cluster 'Intermediate Macrophages' (Figure 3B). Additionally, we identified a TAM cluster that was characterized by the expression of genes involved in phagocytosis (*H2-Ab1*) and the complement cascade (*C1qa*), therefore termed 'C1Q$^+$ TAMs' (Figures 3B and S2B). A second C1Q$^+$ TAM cluster was identified and classified as 'Cycling C1Q$^+$ TAMs' due to the high upregulation of cell cycle genes, including *Mki67* and *Top2a* (Figure 3B). The remaining 'SPP1$^+$ TAMs' cluster identified by the co-expression of *Spp1* and *Arg1,* expressed genes involved in angiogenesis (*Vegfa*) and extracellular matrix remodeling (*Spp1* and *Tnf*) (Figures 3B and S2B). Overall, our findings are in line with the study of Zhang et al., which reported very similar dichotomous functional phenotypes of TAMs in CRC patients[21]. Additionally, Zhang and co-authors predicted a differentiation trajectory of monocytes towards SPP1$^+$ TAMs or C1QC$^+$ TAMs in CRC patients. In line, we identified a strong directional flow from tumor-infiltrating monocytes towards intermediate macrophages, which in turn further branched into two opposite paths, ending either in SPP1$^+$ TAMs or C1Q$^+$ TAMs (Figure 3C). However, the current knowledge regarding the microenvironmental cues that might favor the differentiation of tumor-infiltrating monocytes towards SPP1$^+$ TAMs or C1Q$^+$ TAMs is still very limited. Therefore, we hypothesized that EGCs can contribute to SPP1$^+$ TAM differentiation and quantified the SPP1$^+$ TAMs and C1Q$^+$ TAMs in our EGC co-injection CRC model (Figures 3D and S2C). Strikingly, supplementation of EGCs within the CRC TME resulted in increased SPP1$^+$ TAMs, while no difference was found for C1Q$^+$ TAMs. These data suggest that EGCs might specifically promote SPP1$^+$ TAM differentiation in CRC.

To identify key EGC-derived mediators for SPP1$^+$ TAM differentiation in CRC, we used NicheNet, a computational tool designed to infer relationships between signaling molecules and their target gene expression[22]. By using the genes differentially expressed between SPP1$^+$ TAMs and monocytes as target genes, we prioritized TME-CM EGCs-derived candidate ligands potentially driving this differentiation process. Here, TME-CM EGC-derived IL-6 was identified as the top candidate factor for inducing the SPP1$^+$ TAM phenotype (Figures 3E and 3F). Since IL-6 concentration was prominently

elevated in the supernatant of TME-CM EGCs compared to H-CM EGCs (Figure 3G), we hypothesized that TME-CM EGC-derived IL-6 could directly induce SPP1$^+$ TAM differentiation. By making use of our established *in vitro* model (Figure 3H), we proved that IL-6 neutralization in TME-CM EGC supernatant attenuated the differentiation of monocytes into SPP1$^+$ TAMs, further reflected by reduced SPP1 and ARG1 expression (Figures 3I and S2D-2F). As expected, TME-CM EGCs did not promote C1Q expression in monocytes, suggesting that CRC EGCs specifically favor SPP1$^+$ over C1Q$^+$ TAM differentiation (Figures 3I and S2D). On the contrary, monocyte treatment with TME-CM alone was not able to induce SPP1$^+$ TAM differentiation to the same extent as TME EGCs-CM (Figure S2E).

Altogether, these data highlight an important and previously overlooked interaction between EGCs and TAMs in the CRC TME, where EGC-derived IL-6 might be a key regulator for driving SPP1$^+$ TAM differentiation.

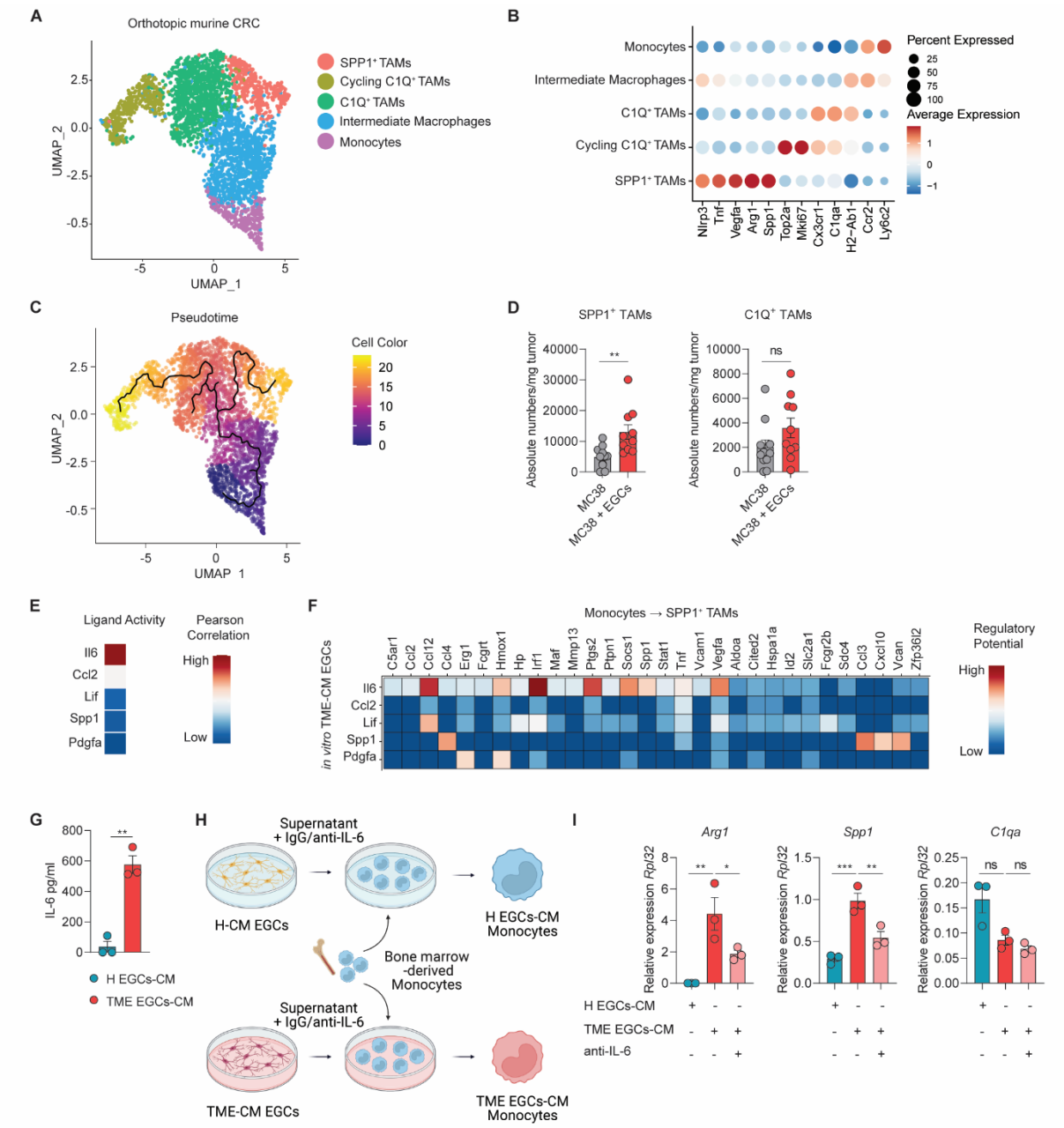

Figure 3. Tumor EGC-derived IL-6 favors SPP1⁺ TAM differentiation.

(A-B) scRNA-seq analysis of monocytes and macrophages from the scRNA-seq data of tumors from BL6 mice bearing orthotopic MC38 tumors, 21d after tumor induction *(n = 3)*. UMAP of tumor-infiltrating monocyte and macrophage subclusters (A) and dot plot of differentially expressed marker genes used for their annotation (B).

(C) Differentiation trajectory of murine CRC-infiltrating monocyte and macrophage subsets inferred by Monocle.

(D) BL6 mice were intracolonically (i.c.) injected with MC38 cells and with or without embryonic neurosphere-derived EGCs (1:1 ratio). SPP1⁺ TAMs and C1Q⁺ TAMs infiltration was assessed on d21. Data represents absolute numbers per mg tumor tissue (*n = 11* MC38, *n = 10* MC38 + EGCs).

(E) Top ligands from *in vitro* tumor microenvironment conditioned medium (TME-CM) EGCs and their Pearson correlation, predicted to be inducing monocytes to SPP1⁺ TAM differentiation according to NicheNet *(n = 3)*.

(F) Heatmap of ligand-target pairs showing regulatory potential scores between top positively correlated prioritized ligands of *in vitro* TME-CM EGCs and their target genes among the differentially expressed genes between monocytes and SPP1^{+} TAMs *(n = 3)*.
(G) IL-6 concentration in the healthy (H)- and TME-EGCs CM *(n = 3)*.
(H-I) *In vitro* murine bone marrow-derived monocytes cultured for 48h with supernatant of H-CM and TME-CM EGCs in the presence or absence of anti-IL-6 (5 µg/mL) *(n = 3)*. Experimental design (H). Relative mRNA levels for *Arg1, Spp1,* and *C1qa* normalized to the housekeeping gene *Rpl32* in monocytes after stimuli (I). All data are represented as mean ± SEM. Statistical analysis: unpaired t-test (D, G) or one-way ANOVA with multiple comparisons (I). * $p < 0.05$, ** $p < 0.005$, *** $p < 0.0005$, ns not significant. See also Figure S2.

Monocyte-derived IL-1 promotes the CRC EGC phenotype

As it is well described that EGCs can adapt their functions according to microenvironmental cues[12,15,23], we aimed at understanding which TME-derived factors could propagate the CRC EGC phenotypic switch. Therefore, considering that colon TME is highly infiltrated by immune cells which have been recently identified as providers of EGC activating factors[12], we questioned if these cells were able to promote this process, thereby generating a positive neuroimmune feedback loop. To investigate the cellular circuits coordinating this interaction, we carried out a NicheNet analysis[22]. Here, tumor immune cell-derived IL-1α and IL-1β were identified as highly ranked ligands to promote the transcriptional shift of H-CM EGCs towards TME-CM EGCs. To investigate if the predicted ligands were part of the TME, we evaluated their presence in healthy colon and orthotopic TME cells. Remarkably, IL-1α and IL-1β were exclusively enriched in the TME samples, while the low ranked ligands TNFα, IFNγ and IL-6 displayed similar or even reduced expression levels in TME versus healthy colonic samples (Figure S3A). Accordingly, a significant increase in the secretion of IL-1β was detected within the TME-CM (Figure 4C). Furthermore, key signature genes of the activated (*Lcn2* and *Timp1*) and immunomodulatory (*Ccl2* and *Il6*) CRC EGC phenotypes were selectively induced both at RNA and protein level in primary murine EGCs after IL-1 treatment (Figures 4D, 4E and S3B; Table S2). In line, blocking IL-1R signaling in EGCs was sufficient to completely abrogate the induction of the CRC EGC key markers upon stimulation with TME-CM (Figure S3C). Overall, these results strongly suggest that IL-1 is essential for the transcriptional switch of EGCs upon exposure to the colonic TME.

In order to narrow down the specific cell type responsible for IL-1 secretion within the TME, we quantified IL-1 expression in both stromal and immune cells (Figures 4F and S3D-S3G). Here, immune cells were identified as the source for IL-1, while no expression could be found in stromal or other non-immune cells (Figure S3G). Further quantification of IL-1 in several immune cell subpopulations at RNA and protein levels highlighted monocytes and macrophages as the main producers of IL-1 (Figures 4F and S3D-S3H). Among them, monocytes were identified as the major IL-1 source. Subsequently, we aimed to further isolate the effect of tumor-infiltrating monocyte-derived IL-1 on the transcriptional reprogramming of EGCs. To this end, we isolated tumor- and bone marrow

(BM)-derived monocytes from mice bearing orthotopic colon tumors and exposed primary glia to their supernatant with or without IL-1R blockade (Figure 4G). Here, the supernatant of tumor monocytes induced a higher expression of CRC EGC marker genes (*Lcn2, Timp1, Ccl2,* and *Il6*) compared to BM-derived monocytes in an IL-1R dependent manner (Figure 4H).

To further test our hypothesis, we made use of our *in vitro* tumor EGC model to compare the impact of C-C chemokine receptor type 2 (CCR2)$^{-/-}$ and CCR2$^{+/+}$ mice-derived orthotopic TME on primary EGCs (Figure S4A). As expected, CCR2^{+} monocytes drove the CRC EGC reprogramming, further reflected by the reduction of CRC EGC marker gene expression (*Lcn2, Timp1, Ccl2,* and *Il6*) in EGCs treated with CCR2$^{-/-}$ TME-CM (Figure 4I). Moreover, in CCR2$^{-/-}$ mice we observed a significant reduction in tumor volume associated with an absence of tumor-infiltrating monocytes (Figures S4B and S4C), consistent with previous findings of Afik et al.[24]. Lastly, since IL-1 expression was significantly decreased in the tumor tissue of CCR2 deficient mice compared to WT mice (Figure 4J), we could prove that monocytes are the major producers of IL-1 in the colon TME. Overall, our findings strongly support the concept that tumor-infiltrating monocyte-derived IL-1 provides remodeling of the neighbouring enteric glia into activated and immunomodulatory CRC EGCs.

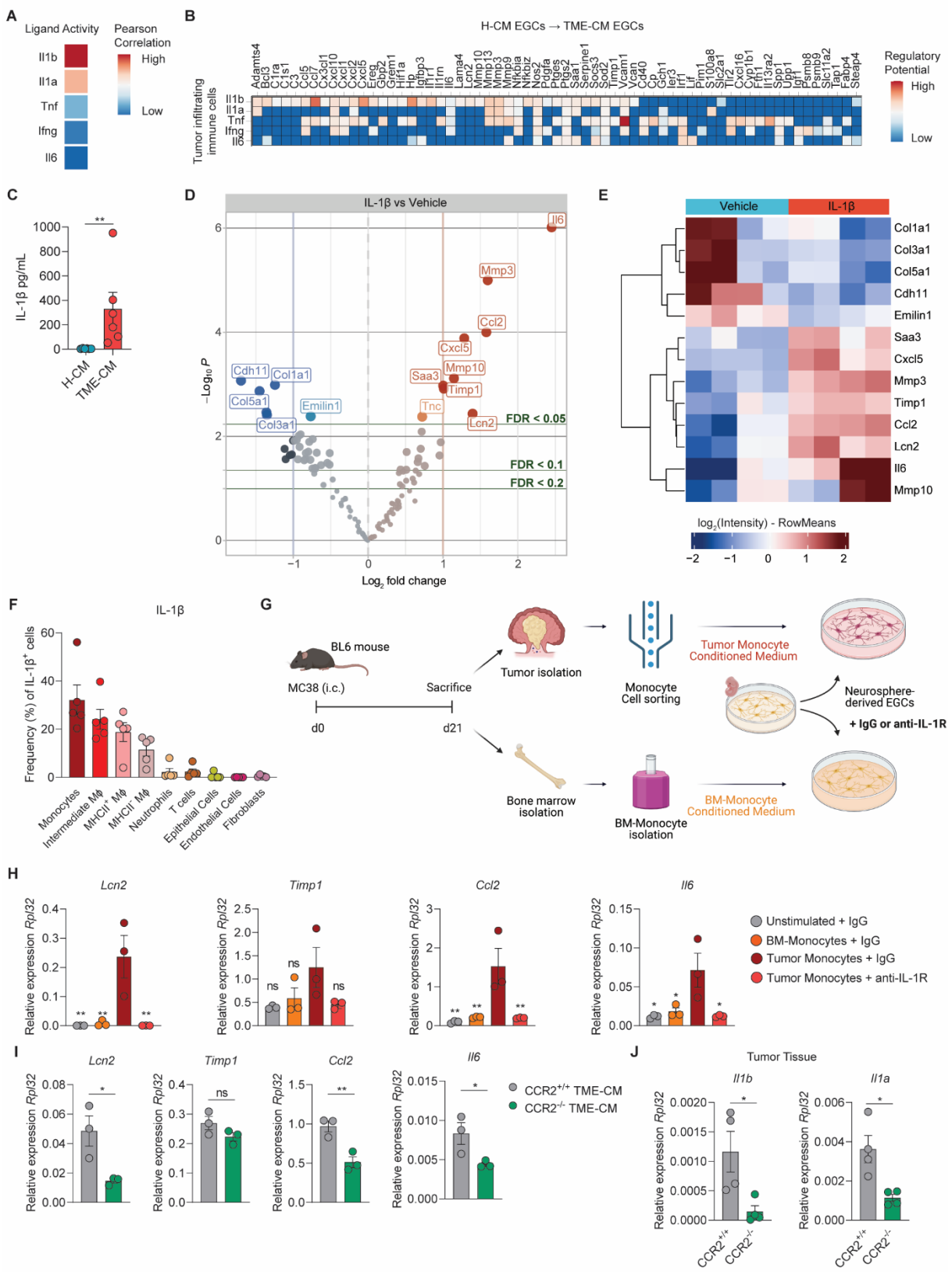

Figure 4. Monocyte-derived IL-1 promotes the CRC EGC phenotype

(A-B) Top ligands from orthotopic CRC tumor-infiltrating immune cells with their Pearson correlation predicted by NicheNet to be inducing CRC EGC signature (A) and heatmap of ligand-target pairs showing regulatory potential scores between top ligands and target genes among the differentially expressed genes between *in vitro* healthy (H) conditioned medium (CM) EGCs and tumor microenvironment (TME)-CM EGCs (B) *(n = 3)*.

(C) Protein level of IL-1β in TME-CM *(n = 6)*.
(D-E) Primary adult EGCs were isolated from BL6 mice and treated with or without IL-1β (10 ng/mL) for 24h. Protein concentration in the culture supernatants was determined by liquid chromatography/mass spectrometry (*n = 4*). Volcano plot (D) and heatmap (E) of differentially expressed proteins between Vehicle and IL-1β-treated EGCs.
(F) BL6 mice were intracolonically injected at d0 with MC38 cells, and both stromal and immune cells were assessed for IL-1β expression at d21. Data are presented as the frequency of total live IL-1β^{+} cells *(n = 5).*
(G-H) Primary embryonic neurosphere-derived EGCs were stimulated for 24h with IgG or anti-IL-1R (5 µg/mL each) with or without the supernatant of sorted tumor monocytes or bone marrow (BM)-derived monocytes from BL6 mice bearing orthotopic CRC tumors. Schematic representation of experimental setup (G). Relative mRNA levels of *Lcn2, Timp1, Ccl2,* and *Il6,* normalized to the housekeeping gene *Rpl32,* in primary embryonic neurosphere-derived EGCs were compared between EGCs stimulated with tumor monocyte supernatant and all other conditions *(n = 3)* (H).
(I) Murine embryonic neurosphere-derived EGCs stimulated with TME-CM of CCR2$^{+/+}$ and CCR2$^{-/-}$ mice for 24h. Relative mRNA levels of *Lcn2, Timp1, Ccl2,* and *Il6* in EGCs, normalized to the housekeeping gene *Rpl32 (n = 3)*.
(J) Relative mRNA levels of *Il1b* and *Il1a* normalized to the housekeeping gene *Rpl32* in murine orthotopic CRC tumors isolated from CCR2$^{+/+}$ and CCR2$^{-/-}$ mice *(n = 3)*. All data are represented as mean ± SEM (C, F, H-J). Statistical analysis: unpaired Mann-Whitney test (C), One-way ANOVA test with correction for multiple comparisons, compared to tumor monocyte supernatant + IgG condition (H) or unpaired t-test (I-J), *p < 0.05, ** p <0.005, ns not significant. See also Figures S3 and S4; Table S2.

IL-1R signaling in EGCs promotes SPP1^{+} TAM differentiation and tumor progression

Subsequently, we aimed at understanding how IL-1R activation in CRC EGCs could shape the TAM populations within the TME. Thus, to assess whether IL-1R blocking in CRC EGCs might directly affect TAM differentiation, we took advantage of our established *in vitro* tumor EGC model (Figure 5A). Here, IL-1R blocking attenuated the differentiation of monocytes into SPP1^{+} TAMs in TME-CM EGCs, further reflected by the reduction of SPP1 and ARG1 expression (Figures 5B, S5A, and S5B). Interestingly, additional neutralization of IL-6 in the supernatant of TME-CM EGCs, pre-treated with anti-IL-1R, did not further affect the SPP1^{+} TAM differentiation (Figure S5C). These findings are in line with the near absence of IL-6 in the supernatant of TME-CM EGCs after IL-1R inhibition (Figure 5C). Altogether these results strengthen our hypothesis on the direct role of the IL-1R/IL-6 axis in CRC EGCs to drive monocyte towards SPP1^{+} TAM differentiation.

To further address the role of IL-1-activated EGCs *in vivo*, we induced inflammation-driven CRC via AOM/DSS in GFAP^{Cre}IL-1R1$^{fl/fl}$ and littermate GFAP^{Wt}IL-1R1$^{fl/fl}$ mice (Figures 5D and S5D). In accordance with our findings in the orthotopic CRC model, immunofluorescence staining showed spatial co-localization of EGCs and TAMs in tumor lesions (Figure 5E). Notably, glial-specific IL-1R deficiency led to a significant reduction of tumor numbers in AOM/DSS-treated GFAP^{Cre}IL-1R1$^{fl/fl}$ compared to littermate GFAP^{Wt}IL-1R1$^{fl/fl}$ mice (Figure 5F). To further address if this phenotype was linked to an alteration in the immunomodulatory function of EGCs, we compared the tumor-infiltrating immune cells of GFAP^{Cre}IL-1R1$^{fl/fl}$ mice with GFAP^{Wt}IL-1R1$^{fl/fl}$ mice subjected to AOM/DSS. Here, the number of

tumor-infiltrating immune cells showed an overall reduction in glial-specific IL-1R deficient mice compared to WT control mice (Figures S5E and S5F). Interestingly, while the number of SPP1^{+} TAMs was decreased in glial-specific IL-1R-KO mice, C1Q^{+} TAM numbers were unaltered, strengthening our hypothesis that CRC EGCs favor the differentiation of infiltrating monocytes towards SPP1^{+} TAMs (Figure 5G).

Taken together, these data provide *in vivo* evidence of the crucial role of EGC-immune crosstalk in CRC, particularly through IL-1R signaling in EGCs, which leads to increased SPP1+ TAM populations and worsened CRC outcomes.

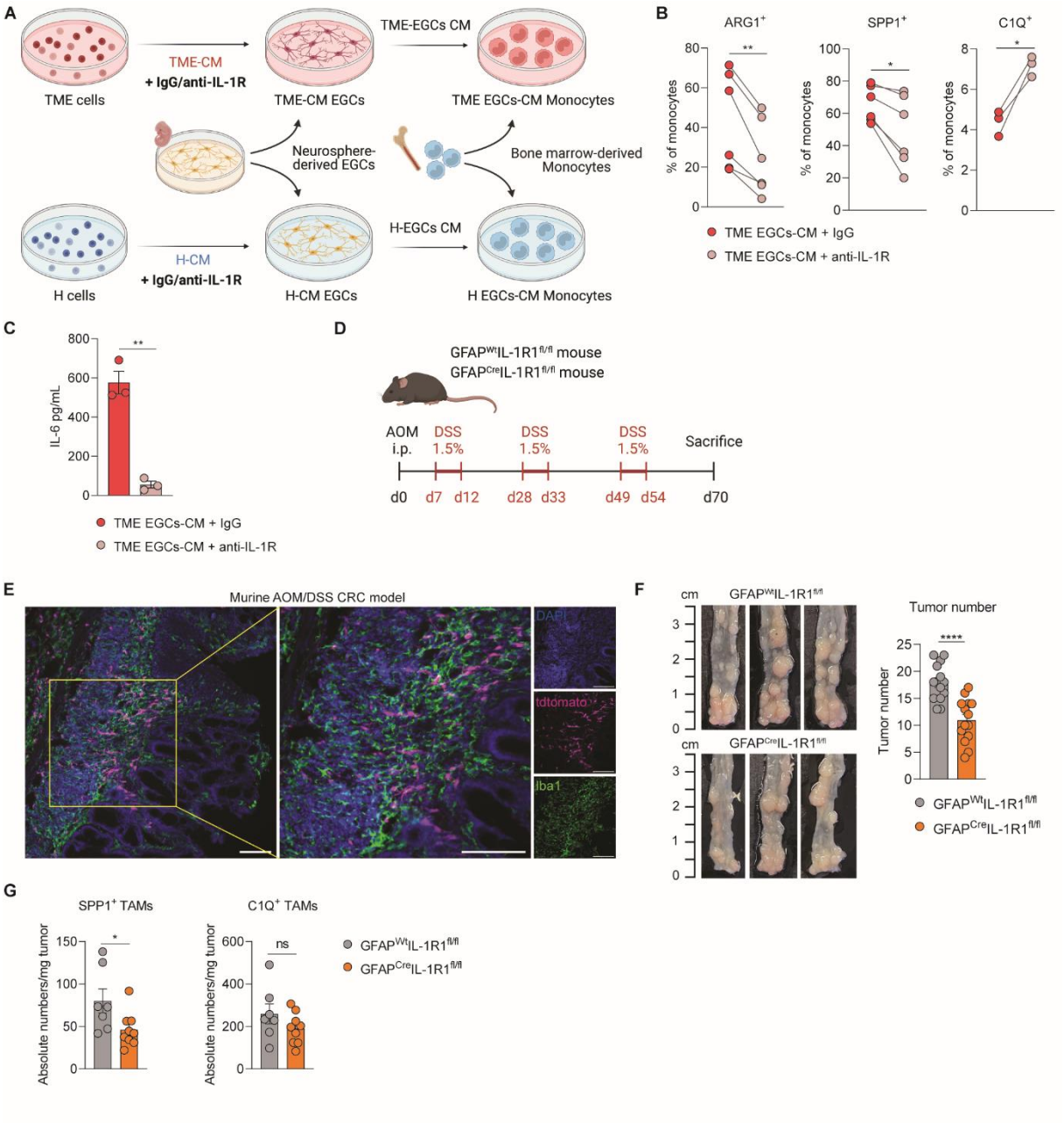

Figure 5. IL-1R signaling in EGCs promotes SPP1^{+} TAM differentiation and tumor progression

(A-C) Murine bone marrow-derived monocytes were cultured for 48h with supernatant of primary embryonic neurosphere-derived EGCs, which were pre-incubated for 24h with tumor microenvironment conditioned medium (TME-CM) with isotype IgG or anti-IL-1R (5 µg/mL each). Experimental design (A). Quantification of ARG1, SPP1 and C1Q expressions in monocytes *(n = 6* ARG1 and SPP1*, n = 3* C1Q*)* (B). IL-6 concentration in the conditioned medium of TME EGCs *(n = 3)* (C).
(D) Schematic representation of experimental set-up of the murine AOM/DSS CRC model. GFAP^{Wt}IL-1R1$^{fl/fl}$ and GFAP^{Cre}IL-1R1$^{fl/fl}$ mice were subjected to an intraperitoneal (i.p.) injection with azoxymethane (AOM, 10 mg/kg body weight) at d0. Starting from d7, mice underwent 3 repetitive cycles of 1.5% dextran sodium sulfate (DSS) in drinking water as indicated. Tumor volume, tumor tissue, and TAMs infiltration were collected or assessed at d70.
(E) Sox10^{CreERT2}Ai14$^{fl/fl}$ mice were i.p. injected with Tamoxifen (1 mg in 100 µL sterile corn oil) on d-7, -6, and -5. Subsequently, mice were subjected to an i.p. injection with AOM (10 mg/kg body weight) at d0. Starting from d7, mice underwent 3 cycles of 2% dextran sodium sulfate (DSS) in the drinking water for 5 days followed by recovery of 16 days. Representative image showing tdtomato (magenta), Iba1 (green) and DAPI (blue) in Sox10^{CreERT2}Ai14$^{fl/fl}$ AOM/DSS murine tumor section at d70, (scale bar 100 µm).
(F-G) GFAP^{Wt}IL-1R1$^{fl/fl}$ and GFAP^{Cre}IL-1R1$^{fl/fl}$ mice were subjected to the AOM/DSS model as described in Figure 5D. Tumor numbers of GFAP^{Wt}IL-1R1$^{fl/fl}$ and GFAP^{Cre}IL-1R1$^{fl/fl}$ littermates with representative images (left) and quantitative comparison of the tumor numbers (right) *(n = 14)* (F). Corresponding absolute numbers of SPP1^{+} and C1Q^{+} TAMs per mg tumor tissue (*n = 7* GFAP^{Wt}IL-1R1$^{fl/fl}$, *n = 9* GFAP^{Cre}IL-1R1$^{fl/fl}$) (G). Data are represented as mean ± SEM (C, F, G). Statistical analysis: paired t-test for (B-C), unpaired t-test (F), and unpaired Mann-Whitney test (G). *p < 0.05, ** p <0.005, **** p <0.005, ns not significant. See also Figure S5.

IL-1R induced-CRC EGC phenotype is conserved in patients affected by CRC

Following our discovery of EGC-immune crosstalk in pre-clinical models of CRC, we sought to determine if a comparable process could also contribute to the disease progression of patients affected by CRC. To achieve this, we initially examined the possible contribution of EGCs in the clinical context by analyzing the colon and rectal cancer dataset from The Cancer Genome Atlas (TCGA- COAD and READ). Here, a high expression of the EGC signature genes, identified in previously published single-cell RNA-seq (scRNA-seq) datasets[19,25,26], was correlated with decreased survival probability in patients affected by CRC (Figures 6A, S6A and S6B). In depth characterization of the patients with high EGC involvement revealed that 79% of this group belonged to the mesenchymal consensus molecular subtype 4 (CMS4)[27], defined by the stromal invasion phenotype (Figure S6C). In comparison, only minor differences were identified when divided based on stage, microsatellite stability, or intrinsic CMS (iCMS) (Figure S6C). These results highlighted an important role for EGCs within the CRC TME.

Next, to assess if the murine CRC EGC transcriptional profile was conserved also in human CRC EGCs, we used the human scRNA-seq KUL3 dataset[25] (Figure S6D), comprising whole CRC lesions and healthy colonic tissues. By comparing gene expression profiles of tumor and healthy EGCs, we identified 589 genes specifically expressed in human CRC EGCs (Figures 6B and S6E; Table S2). Strikingly, among the top differentially expressed CRC EGC genes, we identified the two key murine CRC EGC marker genes *LCN2* and *TIMP1* (Figure 6B). Interestingly, the reactive gene module 7 and the

immunomodulatory gene module 8 which were previously identified to be specifically and differentially expressed in our *in vitro* murine CRC EGCs model, were also similarly upregulated in the human tumor EGC signature. Consistently, the homeostatic gene module 4 was downregulated as well, suggesting an analogous phenotype (Figure 6C). Performing GO term analysis on human EGC subsets, we found that human EGC populations segregate based on the same homeostatic and tumor pathogenesis pathway signatures (Figure 6D), as we observed in our murine EGCs (Figure 2E). Notably, gene set enrichment analysis predicted interaction of human CRC EGCs with TAMs, reflected by enrichment for the GO term "*regulation of macrophage differentiation, activation and migration"* (Figure 6D). Moreover, the colocalization of EGCs and TAMs further supports the idea of a direct interaction in the TME (Figure 6E). In line with this, patients with extensive EGC involvement also display elevated expression of SPP1^{+} TAM signature genes (Figure 6F). Acknowledging the functional analogy between murine and human CRC EGC transcriptomes, we sought to determine whether the molecular and cellular interactions identified in our murine CRC models could be validated in clinical data. Consequently, we employed Ingenuity Pathway Analysis (IPA) to predict the upstream regulators of human CRC EGCs. IPA analysis revealed common upstream regulators as detected for murine CRC EGCs, including TNF, IL-1β, IFNγ, IL-6, and IL-1α (Figures 4A and 6G). Among these factors, IL-1β was the only ligand significantly increased in the TME compared to the healthy colon tissue (Figure 6H). In line with the murine data, cell-population profiling of human CRC samples revealed tumor-infiltrating monocytes as main contributors to IL-1β production (Figures 6I and S6F). Together, these results suggest that similar to our pre-clinical models, IL-1R activation triggers a phenotypical switch in human EGCs, through tumor monocyte-derived IL-1.

Finally, we aimed to determine whether not only the presence of EGCs (Figure 6A) but also their unique CRC-associated phenotype could influence the overall survival of CRC patients. To accomplish this, we utilized our previously published EGC gliosis signature[16], which consists of a specific gene set upregulated in IL-1 activated EGCs. As anticipated, this signature was enriched in both mouse and human CRC EGCs (Figures 2E and 6D). Notably, patients exhibiting higher gliosis gene expression demonstrated a poorer prognosis with reduce overall survival (Figure 6J), highlighting the clinical significance of IL-1R-activated EGCs in CRC. Although additional research is required to confirm the immunomodulatory effects of human CRC EGCs, we observed remarkable parallels between human and murine CRC EGC phenotypes.

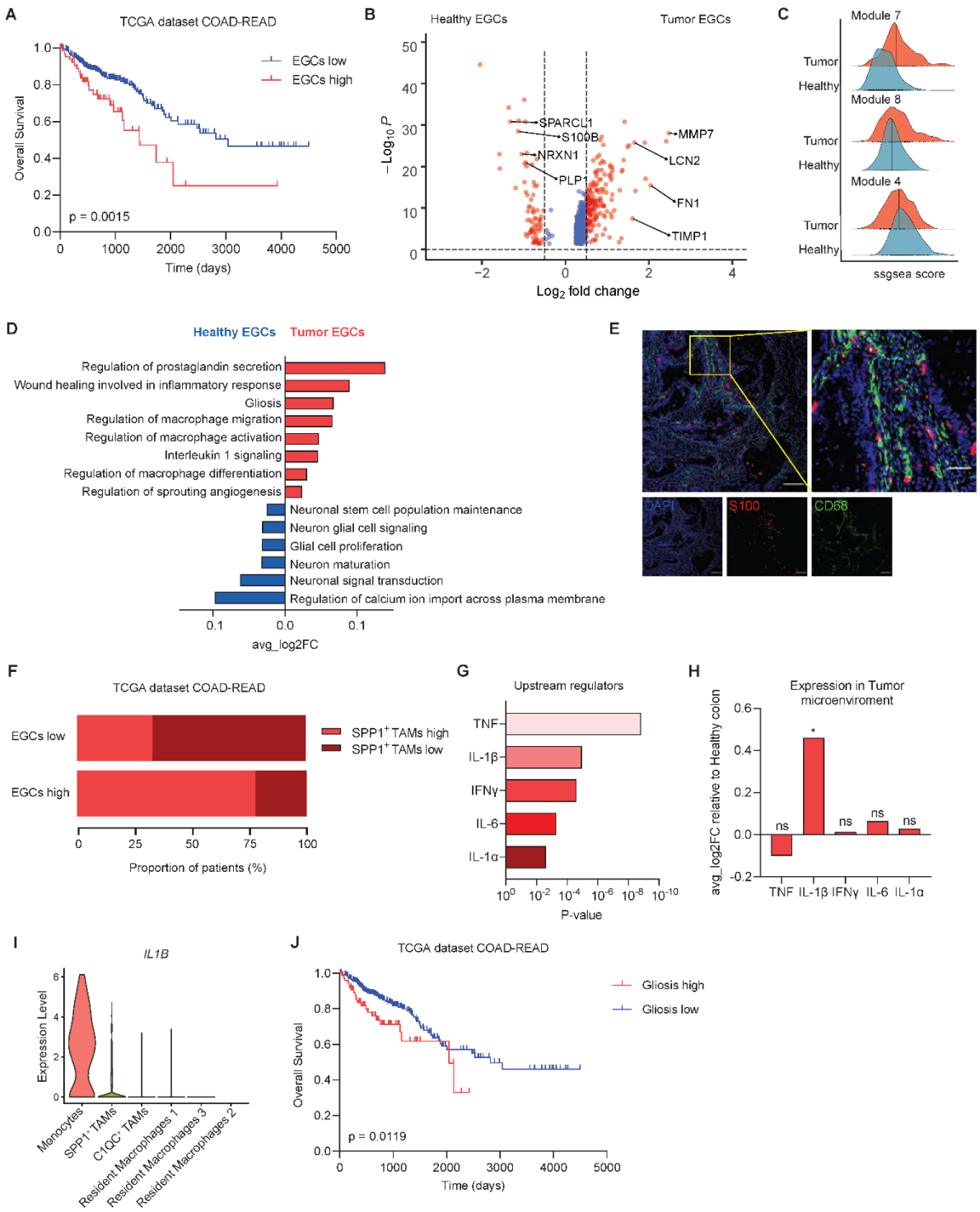

Figure 6. IL-1R induced-CRC EGC phenotype is conserved in patients affected by CRC

(A) Kaplan-Meier overall survival curve for TCGA dataset COAD-READ patients stratified based on their expression of EGCs signature genes (*n = 309* EGCs low, *n = 67* EGCs high).

(B-D) Transcriptome analysis of tumor EGCs in CRC patients (KUL3 Dataset, Lee H. O. et al. 2020, *n = 5*). Volcano plot of differentially expressed genes between healthy and tumor EGCs (B), highlighting genes defining the tumor EGCs signature. Gene Set Enrichment Analysis for murine weighted gene correlation network analysis (WGCNA) modules (Figures 2C and 2D) (C) and GO terms of interest (D).

(E) Representative image showing S100 (red), CD68 (green) and DAPI (blue) in a human CRC tissue section (scale bar 200 µm and 50 µm).

(F) The proportion of EGCs high and low patients of the TCGA dataset COAD-READ classified based on high or low SPP1$^+$ TAMs gene signature expression (*n = 309* EGCs low, *n = 67* EGCs high).
(G-I) Transcriptome analysis of human CRC and healthy colon tissues in the KUL3 Dataset, Lee H. O. et al. 2020 (*n = 5*). Predicted upstream regulators for CRC EGCs signature with their P values (G). Bar plot showing expression of *TNF, IL1B, IFNG, IL6,* and *IL1A* in CRC tumor microenvironment relative to healthy colon samples (H). Violin plot showing expression of *IL1B* in the tumor-infiltrating myeloid cell clusters (I).
(J) Kaplan-Meier overall survival curve for TCGA dataset COAD-READ patients stratified based on their expression of the gliosis signature genes. (*n = 299* gliosis low, *n = 77* gliosis high). Statistical analysis: Mantel cox test (A, J) and Wilcoxon Rank Sum test (H). *$p < 0.05$, ns not significant. See also Figure S6 and Table S2.

DISCUSSION

To date, the overall therapeutic efficacy and the 5-year survival rate for patients with advanced CRC are still low[1]. Hence, a better understanding of the pathogenesis of CRC is crucial to develop new therapeutic strategies along with advanced patient stratification for precision medicine. Our findings reveal important new insights into the CRC microenvironment, as we identified a previously unexplored neuroimmune interaction between EGCs and TAMs. We have uncovered a positive feedback loop in which monocyte-derived IL-1 activates EGCs that, in turn, via IL-6 directly promote the differentiation of tumor-infiltrating monocytes towards SPP1$^+$ TAMs. Importantly, we demonstrate that tumor EGCs present a distinct reactive phenotype induced by IL-1R signaling, which correlates with worse outcomes both in a pre-clinical mouse model and patients affected by CRC.

EGCs are a highly plastic cell type that can modify their functions based on microenvironmental cues[7]. Recent studies have identified specific factors, including IFN-γ, IL-1, and adenosine triphosphate, as triggers of EGC transcriptional reprogramming in both healthy and diseased conditions[12,16,23]. In particular, IL-1-mediated EGC reactivity and its effects on immune cell modulation have been extensively studied in the context of intestinal inflammation[16,28]. However, the mechanisms underlying these processes in CRC are not yet fully understood. Using a combination of murine bulk and human scRNA-seq, our results revealed that EGCs acquire a reactive and highly immunomodulatory transcriptional signature in response to TME-derived IL-1. Interestingly, we identified tumor-infiltrating monocytes as the main source of IL-1 within the tumor. In line, previous *in vitro* experiments published by Valès *et al.*[4] also suggested IL-1 to be important for EGC-cancer stem cell interactions during CRC.

Our study utilizes single-cell and bulk RNA-seq techniques to better understand and predict the interactions between EGCs and TAMs within the colonic TME. Using our murine orthotopic CRC model, we identified two distinct subsets of TAMs with different ontogeny and properties. The C1Q$^+$ TAMs which preferentially express genes involved in phagocytosis and antigen presentation coexist in the TME with SPP1$^+$ TAMs that are enriched for factors regulating angiogenesis and extracellular

matrix, suggesting their key role in colon tumorigenesis. This dichotomy has also been identified in patients with colorectal cancer[21], supporting the relevance of our findings to human disease. Furthermore, we predicted a potential EGCs-TAMs crosstalk and demonstrated that upon IL-1 stimulation, EGCs promoted the differentiation of monocytes towards pro-tumorigenic SPP1$^+$ macrophages via IL-6. Thereby, our study identified EGCs as an additional important actor in SPP1$^+$ TAM differentiation that together with cancer-associated fibroblasts may contribute to tumor progression[29,30]. Recently, pan-cancer transcriptome analysis has identified SPP1$^+$ TAMs as the most pro-tumorigenic macrophage subset in various cancers, including CRC[31]. Hence, inhibiting the differentiation of SPP1$^+$ TAMs may significantly impede tumor progression. In this regard, we demonstrated that blocking IL-1R signaling in EGCs resulted in reduced SPP1$^+$ TAM differentiation and fewer colonic tumor lesions in a mouse model of inflammatory colorectal cancer. In addition, we showed CRC EGCs being functionally associated with myeloid cell migration, as reflected by increased *Ccl2* expression. Considering that the tumor monocyte population decreased upon EGC depletion and after EGC-specific IL-1R signaling blockade, we speculate that CRC EGC-derived chemokines (i.e. CCL2 and CXCL5) could also promote the infiltration of monocytes in the colonic tumor site. This would be in line with our recent findings showing early expression of CCL2 by EGCs in the context of intestinal inflammation[15]. Further research will need to determine whether the pro-tumorigenic role of EGCs is exerted solely on the SPP1$^+$ TAMs or whether other glial-induced factors are at play.

Our research elucidates a molecular pathway involved in glial-immune communication in CRC, which could potentially be of relevance of various tumors exhibiting neuronal infiltration, a factor frequently linked to poorer disease outcomes[32–38]. Apart from EGCs, peripheral glial cells, including Schwann cells, play a crucial role in cancer pathophysiology as shown in pancreatic ductal adenocarcinoma, lung cancer, and in melanoma[39–41]. Consistent with the pro-tumorigenic functions of EGCs in CRC, studies in melanoma models have shown that tumor Schwann cells favor the differentiation of pro-tumorigenic macrophages and enhanced tumor growth[41]. Overall, glial-immune crosstalk might be an overlooked critical component of tumor pathophysiology in many cancer types beyond CRC.

Consistent with the identification of a pro-tumorigenic EGC phenotype in mice, we found that also in patients the CRC EGC transcriptomic signature was associated with reduced overall survival. Therefore, we could speculate that our newly identified CRC EGC gene signature might be used as a potential biomarker to predict disease outcomes. In line with the stromal nature of EGCs, we demonstrated that the vast majority of patients with high EGC involvement belonged to the consensus molecular subtype 4 (CMS4), which is characterized by a mesenchymal-like phenotype, a strong stromal infiltration and the worst overall and relapse-free survival compared to the other CMS subtypes[27]. Gene ontology analysis revealed that also the human tumor glia cells were enriched for

immunomodulatory transcriptional programs related to macrophage differentiation, leading to the assumption that CRC EGC-derived signals modulate TAMs also in patients. Consistently, immune-related pathways, including IL-6 signaling, were enriched in CRC EGCs in a human single-cell data set published by Qi et al.[29]. Additionally, the spatial co-localization of EGCs and SPP1$^+$ TAMs in patient's samples functionally links these two cellular populations in the CRC tissue microenvironment.

In the process of defining a specific EGC phenotype, we successfully demonstrated that our previously published IL-1 gliosis gene signature is associated with poor prognosis in CRC patients[16]. This finding aligns with previous research connecting IL-1R signaling to decreased survival and altered TAM functionality in patients with gastric cancer[42].

In conclusion, our study reveals a critical role for IL-1R signaling in driving enteric glia-macrophage interactions in CRC pathogenesis. Our research provides essential insight into the complex neuroimmune mechanisms underlying the development of this disease, shedding light on potential novel biomarkers and specific therapeutic targets that hold the promise of transforming the management of this devastating disease.

ACKNOWLEDGMENTS

We acknowledge all members of Prof. Matteoli's laboratory and Prof. Wehner´s laboratory for the scientific discussions. We would like to thank Tine Gomers, Karlien Vranken and Renata Siqueira de Mello (TARGID, KU Leuven) and Patrik Efferz and Bianca Schneiker (Department of Surgery, University Hospital Bonn) for technical assistance during experiments. Furthermore, we would like to thank Ally Peddle and Yourae Hong (Molecular Digestive Oncology, Department, KU Leuven), Lukas Ferreira Maciel (Laboratory for Molecular Cancer Biology, VIB-KU Leuven) and Florent Petitprez (MRC Centre for Reproductive Health, University of Edinburgh) for their scientific support on bio-informatic analysis. Within KU Leuven we would like to acknowledge the following core facilities: FACS Core, Genomics Core (UZ Leuven), LiMoNe VIB Bioimaging Core and VIB Center for Brain & Disease Research. We would like to thank the Cell and Tissue Imaging Cluster (KU Leuven) for the usage of the Zeiss LSM 880 – Airyscan (supported by Hercules AKUL/15/ 37_GOH1816N and FWO G.0929.15 to Prof. Pieter Vanden Berghe).We would like to thank the support from the Core Facilities of the Medical Faculty, University of Bonn, specifically the Analytical Proteomics Core, funded by the Deutsche Forschungsgemeinschaft (DFG) – project 386936527, the Bioinformatics Data Analysis Core, and the Next Generation Sequencing Core. BioRender was used for creating graphical images.

V.D.S. was supported by a Stichting tegen Kanker postdoctoral fellowship. S.S. was supported by KU Leuven-University of Melbourne Global PhD (GPUM/22/020). F.B. was supported by the KU Leuven-University of Edinburgh Global PhD (GPUE/20/003). B.K. was supported by the Taiwan - KU Leuven PhD

Scholarship. M.V. was supported by a Fonds voor Wetenschappelijk Onderzoek Vlaanderen (FWO, 11L0822N) PhD fellowship. S.I. was supported by a MSCA-IF (79756–GLIAMAC) and a fellowship from the European Crohn's and Colitis Organization (ECCO). S.V. and S.T. were supported by the FWO grant G067821N and Stichting tegen Kanker grant F/2020/1512. G.M.'s lab was supported by FWO grants G0D8317N, G0A7919N, G086721N, G088816N and S008419N, KU Leuven Internal Funds (C12/15/016 and C14/17/097). S.W. and L.S. were supported by the DFG-funded Immunosensation^2 cluster of excellence EXC2151-190873048. S.W. and R.S. received funding from BONFOR. B.G.R. received funding from the Deutsche Krebshilfe through a Mildred Scheel Nachwuchszentrum Grant (70113307).

AUTHOR CONTRIBUTIONS

Conceptualization, L.V.B., V.D.S., L.S., R.S., S.W. and G.M.; Methodology, L.V.B., V.D.S., L.S., S.W. and G.M.; Software, S.S., S.A., Z.H., J.H., L.V.B. and L.S.; Validation, L.V.B., V.D.S. and L.S.; Formal Analysis, L.V.B., V.D.S., L.S., S.S. and S.A.; Investigation, L.V.B., V.D.S., L.S., S.S., S.A., F.B., L.Z., S.V., B.K., B.G.R., M.T., M.V. and S.I.; Resources, G.M., S.W., S.T. and F.D.S.; Data Curation, L.V.B., V.D.S., L.S., S.S., S.A., S.V., Z.H. and J.H.; Writing – original draft, L.V.B., V.D.S. and L.S.; Writing – review & editing, all; Visualization, L.V.B., V.D.S., L.S., S.S., S.A., and Z.H.; Supervision, G.M., S.W., S.T., F.D.S., R.S., M.S. and V.D.S.; Project administration, L.V.B., V.D.S., L.S., R.S., S.W. and G.M.; Funding acquisition, V.D.S., S.I., G.M. and S.W..

DECLARATION OF INTERESTS

The authors declare no competing interests.

INCLUSION AND DIVERSITY

We support inclusive, diverse, and equitable conduct of research.

METHODS

Materials availability. This study did not generate new unique reagents.

Animals. Female and male mice, age 8-12 weeks, were maintained at the KU Leuven animal facility or at the animal facility of the University of Bonn, medical faculty on a 12:12 hour light–dark cycle and had ad libitum access to tap water and commercially available chow (ssniff® R/M-H, ssniff Spezialdiäten). WT C57BL/6J, PLP1^{CreERT2}iDTR, GFAP^{Cre}IL-1R1$^{fl/fl}$ and Sox10^{CreERT2}Ai14$^{fl/fl}$ mice originated from Jackson Laboratories directly or were bred in our animal facilities. CCR2$^{-/-}$ and CCR2$^{+/+}$ mice were provided by Prof. Philippe Van den Steen. All experimental procedures were approved by the Animal Care and Animal Experiments Ethical Committee of KU Leuven (208/2018 and 213/2018) or by the appropriate authorities of North-Rhine-Westphalia, Germany (81-02.04.2021.A424).

MC38 cell line. Murine colon adenocarcinoma cell line MC38 (NCI, ENH204-FP) was kindly provided by Prof. Max Mazzone (VIB - KU Leuven). The MC38 cell line was maintained in 5% CO_2 at 37°C in high glucose Dulbecco's Modified Eagle Medium (DMEM) (Gibco, ThermoFisher Scientific) supplemented with 10% Fetal Bovine Serum (FBS) (Biowest), 100 µg/mL Penicillin and Streptomycin, 2 mM L-glutamine, 10 mM N-2-hydroxyethylpiperazine-N-2-ethane sulfonic acid (HEPES), 1 mM sodium pyruvate, 50 µM 2-Mercaptoethanol and 1X Non-Essential Amino Acids (all from Gibco, ThermoFisher Scientific).

Embryonic neurosphere-derived enteric glial cells (EGC) culture. Embryonic neurosphere-derived EGCs were obtained as previously described[15]. Briefly, total intestines from E13.5 C57BL/6J mice were digested with collagenase D (0.5 mg/mL; Roche) and DNase I (0.1 mg/mL; Roche) in DMEM/F-12 (Gibco, ThermoFisher Scientific) for 1 hour at 37°C under gentle agitation. After digestion, tissue was filtered through a 70 µm cell strainer and cells were cultured in a CO_2 incubator at 37°C in DMEM/F-12, 100 µg/mL Penicillin and Streptomycin, 2 mM L-glutamine, 10 mM HEPES, 1 mM sodium pyruvate, 50 µM 2-Mercaptoethanol supplemented with 1x B27 (Gibco, ThermoFisher Scientific), 40 ng/mL Epidermal Growth Factor (EGF) (Stemcell Technologies) and 20 ng/mL Fibroblast Growth Factors (FGF) (Invitrogen, ThermoFisher Scientific). After a minimum of 1 week of culture, neurospheres were treated with NeuroCult™ Chemical Dissociation Kit (Stemcell Technologies) according to the manufacturer's protocol and filtered through a 70-µm cell strainer. Cells were seeded on Poly-D-Lysine (PDL solution, 1.0 mg/mL, Sigma Aldrich) coated plates and differentiated in DMEM medium supplemented with 10% FBS, 100 µg/mL Penicillin and Streptomycin, 2 mM L- glutamine, 10 mM HEPES, 1 mM sodium pyruvate, 50 µM 2-Mercaptoethanol (DMEM complete medium) until confluence for 5 days to obtain primary EGCs. For IL-1 stimulation experiments, 5 x 10^4 neurosphere-derived EGCs/mL were stimulated with or without recombinant murine 10 ng/mL IL-1α (Peptrotech) and/or 10 ng/mL IL-1β (Sigma Aldrich) for 24 hours.

Neurosphere-derived adult enteric glial cells (EGC) culture. Neurosphere-derived adult EGC cultures were obtained as described previously[16]. Briefly, small intestines of 8-16 weeks old C57BL/6 mice were harvested, cleansed, cut in 3-5 cm long segments and kept in oxygenated Krebs-Henseleit buffer (126 mM NaCl; 2.5 mM KCl: 25 mM $NaHCO_3$; 1.2 mM NaH_2PO_4; 1.2 mM $MgCl_2$; 2.5 mM $CaCl_2$, 100 IU/mL Penicillin, 100 IU/mL Streptomycin and 2.5 µg/mL Amphotericin). For each segment, the muscularis layer was peeled and collected for digestion. Muscularis tissues were incubated for 15 min in DMEM containing Protease Type 1 (0.25 mg/mL, Sigma-Aldrich) and Collagenase A (1 mg/mL, Sigma-Aldrich) at 37 °C and 150 rpm. Digestion was stopped with DMEM containing 10% FBS (Sigma-Aldrich) and cells were cultured in proliferation medium (neurobasal medium with 100 IU/ Penicillin, 100 µg/mL Streptomycin, 2.5 µg/mL Amphotericin (all ThermoFisher Scientific), FGF and EGF (both 20 ng/mL, Immunotools) at 37°C, 5% CO_2 to promote neurosphere formation. After 1 week in culture, enteric neurospheres were dissociated with trypsin (0.25%, ThermoFisher Scientific) for 5 min at 37 °C and differentiated at 50% confluency on Matrigel (100 µg/mL, Corning) coated 6 well plates for 1 week in differentiation medium (neurobasal medium with 100 IU/ Penicillin, 100 µg/mL Streptomycin, 2.5 µg/mL Amphotericin, B27, N2 (all Thermo Scientific) and EGF (2 ng/mL, Immunotools). For liquid chromatography/mass spectrometry (LC/MS) experiments, mature EGCs were treated with or without IL-1β (10 ng/mL, Immunotools) for 24 hours. Conditioned media were collected and concentrated using Pierce™ Protein Concentrators, 3K MWCO (ThermoFisher Scientific) according to the manufacturer's instructions. After denaturation at 95°C for 5 min, samples were snap-frozen and kept at -80°C until further processing.

***In vitro* tumor EGCs model**. Both orthotopic tumors and healthy colons of C57BL/6J, $CCR2^{+/+}$ or $CCR2^{-/-}$ mice were digested for 30 min in DMEM with 2.5% FBS, 100 µg/mL Penicillin and Streptomycin, 200 U/mL collagenase IV (Gibco, ThermoFisher Scientific) and 125 µg/mL type II dispase (Gibco, ThermoFisher Scientific) to obtain a single-cell suspension. Tumor microenvironment conditioned medium (TME-CM) and healthy colon conditioned medium (H-CM) were generated by culturing 5 x 10^5 cells/mL in DMEM-complete medium overnight. Next, primary murine embryonic neurosphere-derived EGCs were stimulated with the TME-CM or H-CM for 6, 12 or 24 hours. For IL-1R blocking experiments, primary embryonic neurosphere-derived EGCs were incubated for 24h with TME-CM together with 5 µg/mL isotype IgG (BioXCell) or 5 µg/mL anti-IL-1R (BioXCell).

Bone marrow-derived monocyte isolation and stimulation. Murine bone marrow (BM)-derived monocytes were isolated from C57BL/6 mice. Briefly, the tibia and femur were dissected, and BM cells were flushed with DMEM high glucose supplemented with 10% FBS. After cells were collected and counted, monocytes were isolated with the EasySepTM Mouse monocyte isolation kit (Stemcell Technologies) according to the manufacturer's instructions. Next, 5 x 10^5 monocytes were stimulated

for 48 hours with 1 mL of H-CM, TME-CM, or with the supernatant of *in vitro* embryonic neurosphere-derived EGCs pre-incubated for 24h with H-CM or TME-CM. For IL-1R blocking experiments, 5 µg/mL isotype IgG (BioXCell) or 5 µg/mL anti-IL-1R (BioXCell) was removed from the EGCs supernatant by using 20 µL/mL Dynabeads™ Protein G (ThermoFisher Scientific) according to the manufacturer's instructions. For IL-6 neutralization experiments, 20 µL/mL Dynabeads™ Protein G (ThermoFisher Scientific) together with 5 µg/mL anti-IL-6 (R&D Systems) or 5 µg/mL isotype IgG (R&D Systems) was added to the supernatant of H-CM EGCs and TME-CM EGCs and incubated for 2 hours before removal by taking advantage of magnetisation with the DynaMag™-2 Magnet (ThemoFisher Scientific).

Orthotopic CRC model. Orthotopic colonic sub-mucosal implantation of CRC cells was performed as previously described[43]. Briefly, MC38 cells were intracolonically (i.c.) injected as a single-cell suspension containing between 75 000 - 750 000 MC38 cells/ 100 µL PBS dependent on the susceptibility of the mouse strain. Two weeks prior to the start of each experiment, PLP1^{CreERT2}iDTR mice were injected intraperitoneally (i.p.) 2 times every other day with 100 mg/kg Tamoxifen (Sigma-Aldrich) dissolved in 100 µL MIGLYOL®812 (Sigma-Aldrich). For EGCs *in vivo* depletion experiments, PLP1^{CreERT2}iDTR mice were injected i.c. with 2 mg/kg Diphtheria toxin (DT) (Merck, Sigma) dissolved in 100 µL of saline, three and five days prior to the start of the tumor implantation. For the EGCs supplementation model, primary embryonic neurosphere-derived EGCs were isolated with 0.05% Trypsin-EDTA (Gibco, ThermoFisher Scientific) and treated with HBSS (Gibo, ThermoFisher Scientific) supplemented with 100 µg/mL DNAse I (Roche) and 5 mM $MgCl_2$ (Sigma-Aldrich) for 30 min at RT. Subsequently, the EGCs were first washed with HBSS with 5 mM $MgCl_2$ and then with PBS. Finally, EGCs were resuspended in PBS together with MC38 cells in a ratio of 1:1 and orthotopically co-injected in C57BL/6J WT mice. Tumor volume was determined by caliper measurements and calculated based on the height (h), length (l) and width (w) of the tumor, according to the formula: $(\pi/6)*h*l*w$.

AOM-DSS model. Female GFAP^{Cre}IL-1R1$^{fl/fl}$ and GFAP^{Wt}IL-1R1$^{fl/fl}$ mice were subjected to the azoxymethane/dextran sulfate sodium (AOM/DSS) model (modified after[44]) starting at 10-14 weeks of age. In short, i.p. injection of AOM (Sigma-Aldrich) was performed with 10 mg/kg body weight at day 0, and mice were given a 1-week recovery before starting the first 1.5% DSS (MP Biomedicals Germany GmbH) administration at day 7 (in drinking water). DSS water was given for five days, followed by 16 days of recovery in three repetitive cycles (Figure 5D). Mice were sacrificed on day 70 and tumor numbers were determined. Tumor tissue was directly processed for isolation of tumor-infiltrating leukocytes.

For Sox10^{CreERT2}Ai14$^{fl/fl}$ mice subjected to the AOM/DSS model, slight adjustments were made to the above-described protocol. Female Sox10^{CreERT2}Ai14$^{fl/fl}$ mice were i.p. injected with Tamoxifen (MP

biomedicals, 1 mg in 100 µL sterile corn oil) on days -7, -6, and -5. On day 0, the AOM/DSS model was started as described above, but here mice were subjected to a DSS concentration of 2% in drinking water since this strain was less susceptible to DSS. On day 70, colons were harvested and cryo-embedded as swiss rolls for immunohistochemistry.

MILAN multiplex immunohistochemistry of tumor tissue sections of patients with CRC. Multiplex immunohistochemistry and analysis were performed according to a previously published method ([45–47] and https://doi.org/10.21203/rs.2.1646/v5). Briefly, tissue sections (3 µm thickness) were prepared from formalin-fixed paraffin-embedded human CRC samples (collected at the UZ/KU Leuven biobank according to protocol S66460). First, FFPE-tissue slides were deparaffinized by sequentially placing them in xylene, 100% ethanol and 70% ethanol. Following dewaxing, antigen retrieval was performed using PT link (Agilent) using 10 mM Ethylenediaminetetraacetic acid (EDTA) in Tris-buffer pH 8. Immunofluorescence staining was performed using Bond RX Fully Automated Research Stainer (Leica Biosystems) with the primary antibodies rabbit anti-S100B (Dako) and mouse anti-CD68 (Invitrogen, ThermoFisher Scientific). The sections were incubated for 4h with the primary antibodies, washed several times and afterwards stained for 30 min with fluorescently labelled secondary antibodies (Alexa fluor 647 donkey anti-rabbit and Alexa Fluor 488 goat anti-mouse respectively). Slides were then incubated for 10 min with a buffer containing 4,6-diamidino-2-phenylindole (DAPI), after which mounting medium (50% glycerol; 584mM C12H22O11; 10mM Phosphate, 154mM NaCl; pH 7,5) and a coverslip (Agilent, ref. CR12230-7) were manually applied to the slides. Then the slides were scanned using a Zeiss Axio Scan Z.1 (Zeiss) at 10x magnification. Utilize ImageJ (1.53T) and Qu path (0.3.2) were used for the region selection and to subtract background and tissue autofluorescence. Further analysis was performed by using ImageJ.

Immunohistochemistry and Immunofluorescence. Orthotopic tumors were fixed overnight (ON) at 4°C in Periodate-Lysine-Paraformaldehyde (PLP) buffer consisting of Milli-Q Water supplemented with 1% paraformaldehyde, 0.075 M lysine (pH 7.4), 0.037 M sodium phosphate (pH 7.4) and 0.01 M $NaIO_4$ (all from Sigma-Aldrich). Samples were washed three times with Milli-Q Water supplemented with 0.037 M sodium phosphate (pH 7.4), followed by a minimum of 4h incubation in 30% sucrose (VWR chemicals) in PBS. Then, samples were embedded in OCT (Scigen) and stored at -80°C until usage.

Preceding immunohistochemical staining, 7-µm orthotopic tumor tissue sections on SuperFrost Plus™ Adhesion slides (Edpredia) were exposed to two washes with HistoChoice Cleaning Agent for 2 min each (Sigma-Aldrich) and subsequent hydration with Ethanol 100% for 2 min each (Merck) followed by deionized water. Then haematoxylin and eosin (both from Leica) staining was performed using

standard procedures. Imaging was performed with Nikon Marzhauser Slide Express2, processed and analysed using ImageJ.

Preceding immunofluorescent staining, tissues were sectioned to 7-µm thickness on SuperFrost Plus™ Adhesion slides (Edpredia) and blocked with blocking buffer (PBS containing 0.02% Sodium azide (Sigma-Aldrich), 0.3% donkey serum (Jackson), and 3% Bovine Serum Albumin (BSA, Serva) for 2h at room temperature (RT). Subsequently, samples were incubated ON at 4°C with the following primary antibodies: 1:500 rat anti-F4/80, BioRad and/or 1:300 rabbit anti-GFAP Dako in staining buffer (blocking buffer supplemented with 0.3% Triton X-100 (ThermoFisher, Scientific)). Then, samples were washed in PBS and incubated with DAPI (4',6-Diamidine-2'-phenylindole dihydrochloride; Sigma-Aldrich) combined with the secondary antibodies: 1:1000 donkey anti-rat AF488 (Invitrogen, ThermoFisher Scientific), and/or 1:400 donkey anti-rabbit Cy5 (Jackson) in staining buffer for 2h at RT. Finally, samples were rinsed three times in PBS and mounted with SlowFade Diamond Antifade mounting (Invitrogen, ThermoFisher Scientific). Imaging was performed on the ZEISS LSM 880 confocal microscope and the pictures were analysed using ImageJ.

For immunofluorescent staining of AOM/DSS swiss rolls of $Sox10^{CreERT2}Ai14^{fl/fl}$ mice were fixed ON at 4°C in 4% PFA. Samples were washed once with PBS followed by ON incubation at 4°C in 30% sucrose (Sigma) in PBS. Subsequently, swiss rolls were embedded in Tissue-Tek® O.C.T.™ Compound (Sakura) and stored at -80°C until usage.

Prior to immunofluorescent staining, AOM/DSS samples were sectioned to 14 µm thickness on Superior™ HistoBond™ slides (Marienfeld). Slides were washed three times in PBS, incubated for 10 min in 0.2% Triton X-100 (AppliChem) in PBS, and blocked with blocking buffer (PBS containing 3% donkey serum and 0.1% Triton X-100) for 1h at RT. Subsequently, primary antibody staining was performed ON at 4°C with rabbit anti-Iba1 (1:400, Abcam) in staining buffer (blocking buffer diluted with PBS in a 1:1 ratio). Slides were washed three times in PBS and secondary antibody staining was performed for 2h at RT with donkey anti-rabbit FITC (1:800, Dianova) in staining buffer. After three more washes with PBS, slides were incubated with DAPI (Sigma-Aldrich) for 5 min at RT. After a final wash with PBS, slides were mounted with Shandon™ Immu-Mount™ (Epredia). Imaging was performed on the Nikon ECLIPSE Ti2 microscope using NIS-Elements AR software (version 5.41.01) and pictures were analysed using ImageJ.

Enzyme-linked Immunosorbent Assay (ELISA). Healthy and tumor conditioned medium EGCs supernatants were collected and analysed for IL-6 and IL-1β content using sensitive commercial ELISA kits (R&D Systems, Minneapolis, MN and V-Plex Pro-inflammatory panel Meso Scale Discovery; MSD

respectively) according to the manufacturer's instructions. The data were analysed with the Discovery Workbench 4.0 software (MSD).

Western Blot. Total proteins were extracted from mouse colonic tissues in T-PER buffer (ThermoFisher, Scientific) supplemented with 1 mM dithiothreitol, 10 mg/mL aprotinin, 10 mg/mL leupeptin, 1 mM phenylmethylsulfonyl fluoride, 1 mM Na3VO4 and 1 mM NaF (all from ThermoFisher, Scientific), by homogenization for 1 minute at 30 Hz (TissueLyser II, Qiagen). Lysates were clarified by centrifugation at 4 °C, 12000 g for 30 min and separated on sodium dodecyl sulphate (SDS)-polyacrylamide gel electrophoresis. Blot was incubated with the GFAP antibody (1:500 final concentration, Cell Signaling) followed by a secondary antibody conjugated to horseradish peroxidase (1:5000 final dilution; both from Dako Agilent Technologies). To ascertain equivalent loading of the lanes, the blot was stripped and incubated with an anti-vinculin antibody (1:5000 final dilution, Sigma-Aldrich). Computer-assisted scanning densitometry (GE Healthcare ImageQuant LAS 4000 Luminscent Image Analyzer) was used to analyze the intensity of the immunoreactive bands.

Liquid Chromatography/Mass Spectrometry (LC/MS). LC/MS analysis of adult neurosphere-derived EGC supernatants treated with or without IL-1β was performed by the Core Facility Analytical Proteomics of the University of Bonn as described in the following. All chemicals from Sigma unless otherwise noted. For LC/MS sample preparation, 70 µg of protein per sample was subjected to in-solution preparation of peptides with the iST-NHS 96x sample preparation kit (Preomics GmbH, Martinsried, Germany) according to the manufacturer's recommendations. 0.4 mg TMT10plex isobaric Mass Tag Labeling reagent (Thermo Scientific) was added to each sample and incubated at room temperature for 1 hour. 10 µL 5% hydroxylamine was used to quench the reaction. The preparation procedure was continued according to the iST-NHS kit instructions. Peptide concentration was determined with a colorimetric peptide assay (Thermo Scientific). Equal amounts of peptides were pooled and dried in a vacuum concentrator, dissolved in 20 mM ammonium formate (pH 10) and fractionated by reversed phase chromatography at elevated pH with a Reprosil 100 C18 column (3 µm 125 x 4 mm, Dr. Maisch GmbH, Ammerbuch-Entringen, Germany). 60 fractions were combined into 6 pools and dried in a vacuum concentrator.

Before measurement, peptides were re-dissolved in 0.1% formic acid (FA) to yield a 1 g/L solution and separated on a Dionex Ultimate 3000 RSLC nano HPLC system (Dionex GmbH, Idstein, Germany). The autosampler was operated in µL-pickup mode. 1 µL was injected onto a C18 analytical column (self-packed 400 mm length, 75 µm inner diameter, ReproSil-Pur 120 C18-AQ, 1.9 µm, Dr. Maisch). Peptides were separated during a linear gradient from 5% to 35% solvent B (90% acetonitrile, 0.1% FA) at 300 nL/min during 150 min. The nano-HPLC was coupled online to an Orbitrap Fusion Lumos Mass

Spectrometer (Thermo Fisher Scientific, Bremen, Germany). Peptide ions between 330 and 1600 m/z were scanned in the Orbitrap detector every three seconds with a resolution of 120,000 (maximum fill time 50 ms, AGC target 100%). From MS3-based quantification, peptides were subjected either to collision induced dissociation for identification (CID: 0.7 Da isolation, normalized energy 30%) and fragments analyzed in the linear ion trap with AGC target 50% and a maximum fill time 35 ms, rapid mode. Fragmented peptide ions were excluded from repeat analysis for 30 s. The top 10 fragment ions were chosen for synchronous precursor selection and fragmented with higher energy CID (HCD: 3 Da MS2 isolation, 65% collision energy) for detection of reporter ions in the Orbitrap analyzer (range 100-180 m/z, resolution 50,000, maximum fill time 86 ms, AGC target 200%). Alternatively, peptides were only fragmented by HCD and fragment ions and reporter ions analyzed in the same spectrum (Orbitrap resolution 50,000).

Raw data processing and database search were performed with Proteome Discoverer software 2.5.0.400 (Thermo Fisher Scientific). Peptide identification was done with an in-house Mascot server version 2.8.1 (Matrix Science Ltd, London, UK). LC/MS data were searched against the Uniprot reference proteome mouse database (2022/05, 63628 sequences) and contaminants database (cRAP1)[48]. Precursor Ion m/z tolerance was 10 ppm, fragment ion tolerance 0.5 Da (CID). Tryptic peptides with up to two missed cleavages were searched. C6H11NO-modification of cysteines (delta mass of 113.08406) and TMT10plex on N-termini and lysines were set as static modifications. Oxidation was allowed as dynamic modification of methionine. Mascot results were evaluated by the Percolator algorithm version 3.02.12 as implemented in Proteome Discoverer[49]. Spectra with identifications above 1% q-value were sent to a second round of database search with semi tryptic enzyme specificity (one missed cleavage allowed). Protein N-terminal acetylation, methionine oxidation, TMT10plex, and cysteine alkylation were then set as dynamic modifications. Actual FDR values were 0.2% (peptide spectrum matches) and 0.9% (peptides). Reporter ion intensities (most confident centroid) were extracted from the MS3 level, with SPS mass match >65%.

The statistical analyses of the peptide-spectrum match (PSM) level data were done by the Core Unit for Bioinformatics Data Analysis of the University of Bonn. Analyses were carried out in R environment (R version 4.2) using an in-house developed workflow. Non-unique peptides and single-hit proteins (proteins identified/quantified by only one peptide) were filtered-out prior to the statistical analysis. From all available fractions, only those with the least number of missing values per feature and maximum average intensity across all TMT labels were selected. The PSM-level data were then log-transformed and scaled such that all the samples have the same median values (median normalization method). Next, the normalized data was aggregated to protein-level by applying the Tukey's median polish method. The statistical analysis was performed using the R package limma[50]. For each statistical

contrast, the resulting P-values were adjusted for multiple testing. The false discovery rates (FDR) were calculated by the Benjamini-Hochberg method.

Isolation of tumor-infiltrating leukocytes. Tumor-bearing mice were sacrificed at the described time points. After peeling off the muscularis layer from the orthotopic tumors, tissues were first cut in 1 mm pieces, and then went under mechanical and enzymatic digestion for 30 min in DMEM with 2.5% FBS, 100 µg/mL Penicillin and Streptomycin, 200 U/mL collagenase IV (Gibco, ThermoFisher Scientific) and 125 µg/mL type II dispase (Gibco, ThermoFisher Scientific). AOM/DSS induced tumors and healthy colon samples were peeled off the muscularis layer and underwent epithelial removal by vigorous shaking in Hanks' balanced salt solution (HBSS) with phenol red (Gibco, ThermoFisher Scientific) containing 1% FBS, 100 µg/mL Penicillin and Streptomycin, 1 mM EDTA (Invitrogen, ThermoFisher Scientific) and 1 mM dithiothreitol (DTT) (Sigma- Aldrich) for 8 min at 37°C. A second incubation step was performed for 8 min at 37°C in the same medium without DTT. After washing in wash medium (DMEM with 2.5% FBS and 100 µg/mL Penicillin and Streptomycin), the remaining tissue was cut into small pieces and digested for 30 min at 37°C in pre-warmed alpha Minimum Essential Medium (MEM) (Lonza) containing 5% FBS, 100 µg/mL Penicillin and Streptomycin, 5 U/mL DNase (Roche), 1 mg/mL dispase (Gibco, ThermoFisher Scientific), 1.25 mg/mL Collagenase D (Roche) and 0.85 mg/mL Collagenase V (Sigma-Aldrich). Independent of tumor origin, cells were then filtered through a 70-µm cell strainer (BD Falcon), washed with PBS, and stained with fluorophore-conjugated antibodies.

FACS staining and analysis. Single-cell suspensions (obtained as described above) were incubated for 15 min with mouse FcR Blocking Reagent (1:100 BD Pharmingen) at 4 °C. Next, cells were stained for surface markers (see Methods Table 1 for antibodies list) and incubated for 20 min incubation at 4 °C, then cells were washed with FACS buffer (0.5% FBS and 2 mM EDTA in PBS) and resuspended in FACS buffer containing the viability marker 7-AAD (1:100 BD Pharmingen) before filtering through a 70-µm strainer.

For the intracellular measurement of IL-1α and IL-1β, single-cell suspensions were pre-cultured in DMEM with 2.5% FBS, 100 µg/mL Penicillin and Streptomycin and stimulated with BD GolgiStop™ (1:1000, BD Biosciences) for 4 h in 5% CO_2 at 37°C followed by a pre-incubation with the viability dye eFluor 506 (1:400 eBioscience) for 20 min at 4°C. Then cell suspensions were washed, blocked with FcR Blocking Reagent (1:100 BD Pharmingen) and stained with surface antibodies (see Methods Table 1 for antibodies list) as described above. After a washing step with FACS buffer, cells were incubated for 45 min in Fix/Perm buffer (eBioscience, Invitrogen, ThermoFisher Scientific), followed by 5 min incubation in 1X Permeabilization buffer (eBioscience, Invitrogen, ThermoFisher Scientific). Next, the cells were stained for a minimum of 1 h in 1X Permeabilization buffer containing FcR Blocking Reagent (1:600 BD Pharmingen) and intracellular markers (see Methods Table 1 for antibody details). Cells were

subsequently washed and resuspended in Permeabilization buffer before filtering through a 70-µm strainer.

For cell counting goals, counting beads (1:100 Spherotech) were added per sample. Flow cytometry analyses were performed on a BD Symphony A5 Cell Analyzer (BD Biosciences) and subsequently analysed using FlowJo v.10.6.1.

Methods Table 1. FACS Antibodies

Anti	Conjugate	Company	Cat. No.	Clone
ARG1	Pe-Cy7	eBioscience	25-3697-82	A1efF5
C1Q	FITC	Tebubio	7501F	RmC7H8
CD11b	BUV395	BD Horizon	563553	M1/70
CD11b	PE-Cy7	BD Pharmingen	552850	M1/70
CD19	PE-Cy5	eBioscience	15-0193-82	eBio1D3
CD3	Alexa Fluor 700	BioLegend	100215	17A2
CD31	BV421	BioLegend	102423	390
CD326	PE-Cy7	BioLegend	118215	G8.8
CD3e	eFluor 450	eBioscience	48-0032-82	17A2
CD4	BV605	BioLegend	100548	RM4-5
CD44	AF700	BioLegend	103026	IM7
CD45	BUV805	BD OptiBuild	748370	30-F11
CD45	APC-eFluor 780	eBioscience	47-0451-82	30-F11
CD64	BV711	BioLegend	139311	X54-5/7.1
CD8a	APC-Cy7	eBioscience	25-5773-82	FJK-16s
FOXP3	PE-Cy7	eBioscience	12-5773-82	FJK16S
GP38 (PDPN)	Alexa Fluor 488	BioLegend	127405	8.1.1
IL-1α	PE	BioLegend	503203	ALF-161
IL-1β (Pro-form)	APC	eBioscience	17-7114-80	NJTEN3
Live Dead	eFluor 506	eBioscience	65-0866-14	
Live Dead	7-AAD	BD Pharmingen	51-68981E	
Ly6C	BV421	BioLegend	128043	HK1.4
Ly6C	BV650	BioLegend	128049	HK1.4
Ly6C	FITC	BD Pharmingen	553104	AL-21
Ly6G	BUV563	BD Horizon	612921	IA8
Ly6G	APC	BD Pharmingen	560599	1A8
MHCII	APC-eFluor 780	eBioscience	47-5321-82	M5/114.15.2
MHCII	BV510	BioLegend	107636	M5/114.15.2
SiglecF	eFluor 660	eBioscience	50-1702-80	1RNM44N
SPP1	PE	R&D systems	IC808P	

Tumor-infiltrating monocyte sorting for EGCs stimulation. Tumor-infiltrating monocytes were sorted from orthotopic tumors based on the expression of the viability marker 7-AAD, CD45, CD64, Ly6C, MHCII, SiglecF and Ly6G (see Methods Table 1 for antibodies details) using a Sony MA9000 sorter.

Next, $1x10^5$ tumor or BM-derived monocytes were cultured in complete DMEM medium overnight in 5% CO_2 at 37°C. The conditioned medium of these monocytes was collected and used to stimulate primary embryonic neurosphere-derived EGCs ($5x10^4$ cells/mL) in the presence of 5 µg/mL IgG (BioXCell) or 5 µg/mL anti-IL-1R (BioXCell) for 24h in 5% CO_2 at 37°C.

RNA extraction and gene expression. RNA was isolated using the innuPREP RNA Mini Kit (Analytik Jena) or RNeasy Mini Kit (Qiagen) for tissue and high cell numbers or RNeasy Plus Micro Kit (Qiagen) for low cell numbers according to the manufacturer's instructions. Dependent on RNA concentrations, total RNA was transcribed into cDNA by the qScript™ cDNA SuperMix (QiantaBio) or the High-Capacity cDNA Reverse Transcription Kit (ThermoFisher Scientific) according to manufacturer's instructions. RT-PCR was performed with the LightCycler 480 SYBR Green I Master (Roche) on the Light Cycler 480 (Roche). Results were quantified using the $2^{-\Delta Ct}$ method. The expression levels of the genes of interest were normalized to the expression levels of the reference gene *Rpl32*.

Methods Table 2. Primer Sequences

	Forward primer	Reverse primer
Arg1	CAGAAGAATGGAAGAGTCAG	CAGATATGCAGGGAGTCACC
C1qa	ATCCAGTTTGATCGGACCAC	CATCTTCAGCCACTGTCCATA
Ccl2	CAGGTGTCCCAAAGAAGCTGTA	CATTTGGTTCCGATCCAGG
Ifng	TCAAGTGGCATAGATGTGGAAGAA	TGGCTCTGCAGGATTTTCATG
Il1a	GAGAGCCGGGTGACAGTATC	ACTTCTGCCTGACGAGCTTC
Il1b	TTGACGGACCCCAAAAGATG	AGGACAGCCCAGGTCAAAG
Il6	CCATAGCTACCTGGAGTACATG	TGGAAATTGGGGTAGGAAGGAC
Lcn2	CGGAGCGATCAGTTCCGGG	GCCCTGGTCCTGGTCCCTGA
Rpl32	AAGCGAAACTGGCGGAAAC	TAACCGATGTTGGGCATCAG
Spp1	AGCTCTGCTTGTTACAAAGCC	CAGGTCTTCCAATCTGGATGC
Timp1	AGACAGCCTTCTGCAACT	CAGCCTTGAATCCTTTTAGCATC
Tnfa	CTATGGCCCAGACCCTCACACTC	GCTGGCACCACTAGTTGGTTGTCTT

Bulk RNA sequencing. For Bulk RNA-seq of the *in vitro* tumor EGCs model, total RNA from *in vitro* generated unstimulated, H-CM and TME-CM primary embryonic neurosphere-derived EGCs was provided to the Genomics core (KU Leuven). QuantSeq 3' mRNA libraryprep (015, Lexogen) was used to generate cDNA libraries, followed by sequencing on the HiSeq4000 system. Quality control of raw reads was performed with FastQC v0.11.7 (Andrews S. FastQC: a quality control tool for high throughput sequence data. Available online at: http://www.bioinformatics.babraham.ac.uk/projects/fastqc, 2010.). Adapters were filtered with ea-utils fastq-mcf v1.05 (Erik Aronesty. ea-utils: Command-line tools for processing biological sequencing data. Available online at: https://github.com/ExpressionAnalysis/ea-utils, 2011.). Splice-aware

alignment was performed with HISAT2[51] against the reference genome mm10 using the default parameters. Reads mapping to multiple loci in the reference genome were discarded. Resulting BAM alignment files were handled with Samtools v1.5[52]. Quantification of reads per gene was performed with HT-seq Count v0.10.0, Python v2.7.14[53]. Count-based differential expression analysis was done with R-based (The R Foundation for Statistical Computing, Vienna, Austria) Bioconductor package DESeq2[54]. Reported p-values were adjusted for multiple testing with the Benjamini-Hochberg procedure, which controls false discovery rate (FDR). Data visualization was prepared using ggplot2 R package (v3.4.1) or pheatmap (v1.0.12).

Weighted gene correlation network analysis (WGCNA). First, variance stabilizing transformation was performed on the bulk RNA-seq data generated from unstimulated, H-CM and TME-CM primary neurosphere-derived EGCs using the DESeq2[54] package in R (v4.2.2). Next, WGCNA[55] was performed using the R package WGCNA (v1.72.1). To distinguish the modules with different expression patterns, a soft threshold power of 12, which was the lowest power for the scale-free topology fit index on 0.85, was selected to produce a hierarchical clustering tree (dendrogram). The function "blockwiseModules" was used for automatic block-wise network construction and module identification. The number of modules was detected automatically by the algorithm, with the number of genes in a module limited to between 30 and 5000 genes. The co-expression networks were created based on the similarity of expression patterns of genes and the networks were established by merging genes with similar co-expression patterns into modules.

Single cell RNA sequencing of orthotopic murine Tumors. Cell suspensions of orthotopic murine tumors were processed with a 10x Chromium Next GEM Single Cell 5' kit and loaded on a 10x chromium controller to create Single Cell Gel beads in Emulsion (GEM). A cDNA library was created using a 10x 5' library kit and was then paired-end sequenced on an Illumina Novaseq device following 10x's guidelines (https://www.10xgenomics.com/support/single-cell-immune-profiling/documentation/steps/sequencing/sequencing-requirements-for-single-cell-v-d-j). Sample demultiplexing and data analysis was performed using 10x's Cellranger suite (https://support.10xgenomics.com/single-cell-vdj/software/pipelines/latest/using/vdj) using the standard parameters.

Single-cell RNA sequencing Clustering and Dimensionality reduction. The count matrices obtained after pre-processing with Cellranger were concatenated to obtain a combined raw count matrix which was then analyzed using the Seurat R package (v3.1.3). Cells with less than 300 or more than 6000 genes and cells with more than 15% mitochondrial genes were discarded from the analysis. Normalization and scaling were done with default variables with top variable genes identified using

FindVariableFeatures function. After principal component analysis, 1st 39 principal components were used based on the elbow plot for creating a nearest neighbor graph using FindNeighbours function in Seurat. After clustering at a resolution of 1, clusters were classified into immune and non-immune clusters. 6 small doublet clusters with markers of two or more distinct cell types were removed. Also, two clusters with low nUMI and lacking distinguishing markers of any cell types were also removed. A subset of Seurat Object with immune clusters alone was created and the same pipeline was followed from Normalization to Clustering (number of principal components used = 32). After clustering at resolution 1, the clusters were manually annotated inspired by Zhang et al.[21]. Clusters annotated as monocytes or macrophages were re-clustered similarly to identify the subclusters. These sub-clusters were annotated manually based on the expression of Ly6c2, Ccr2, H2-Ab1, Spp1, C1qa, Cx3cr1, and Mki67. Further to learn potential differentiation trajectory, Monocle-3 was used. (Parameters: n center = 300, minimal branch length = 10, nn.k = 20). Genes upregulated or downregulated in $SPP1^+$ TAMs compared to $C1Q^+$ TAMs were functionally annotated using universal enrichment function 'enricher' from the 'ClusterProfiler' package (v4.6.0) with a gene annotation database aggregation containing all terms from Human Phenotype, Transcription factor, and Hallmark from Molecular Signature Database (MSigDB), BIOCARTA, REACTOME, GO and KEGG Markers for different clusters were determined using a Wilcoxon rank sum test with FindMarkers or FindAllMarkers functions in Seurat.

Inferring cell-cell communication using NicheNet. NicheNet (nichenetr R package; v1.1.0) was used to study the interactions between EGCs and tumor-infiltrating monocytes. To identify TME EGC-derived ligands potentially inducing the differentiation of monocytes into $SPP1^+$ TAMs, bulk RNA-seq data from *in vitro* TME-CM EGCs was used. Ligands were identified after filtering for genes upregulated in 24h time point TME-CM EGCs with respect to 24h timepoint H-CM EGCs (adjusted p value < 0.05). Genes differentially expressed between $SPP1^+$ TAMs and monocytes (adjusted p value < 0.05) were considered as the gene set of interest.

NicheNet was also used to study the interaction between tumor-infiltrating immune cells and EGCs. To identify immune cell-derived ligands potentially inducing differentiation of 24h time point H-CM EGCs into 24h time point TME-CM EGCs, scRNA-seq data of the immune compartment of the *in vivo* murine orthotopic CRC model was used. Using get_expressed_genes function from NichenetR, genes expressed in at least 5 % of immune cell clusters were considered as potential ligands. Genes differentially expressed between TME-CM EGCs and H-CM EGCs (adjusted p value < 0.001) were considered as the gene set of interest.

Bio-informatic analysis: **KUL3 Dataset.** Bio-informatic analysis of the CRC tumor microenvironment of patients affected by CRC was performed making use of the published KUL3 dataset[25]. Integration of

the data, dimensionality reduction, unsupervised clustering and differential gene expression analysis was performed in R using Seurat with SCTransform - Integration pipeline. For downstream analysis, "border" and "tumor" samples were taken together and considered as tumor samples. Patient KUL31 was excluded from all EGCs analysis, due to extremely low cell numbers. Pathway enrichment analysis was done using Ingenuity pathway Analysis (IPA, Qiagen). Modules identified using WGCNA on mouse bulk RNA-seq data was converted to one-to-one human orthologs and then used for single-sample Gene Set Enrichment Analysis GSEA (ssGSEA) as implemented in single-cell Gene Set Variation Analysis (scGSVA) R package (v0.0.11).

TCGA analysis: data acquisition, patients' classification and survival analysis. The processed gene expression RNA-seq (IlluminaHiSeq) data of the Cancer Genome Atlas (TCGA) colorectal adenocarcinoma (COADREAD) was downloaded from University of California SantaCruz (UCSC) Xena using the UCSCXenaTools (ref: https://joss.theoj.org/papers/10.21105/joss.01627) R library. The details of data integration and processing are described in UCSC-Xena browser (https://xenabrowser.net/). The clinical information and overall survival (OS) data of the patients were also obtained using UCSCXenaTools (data subtype: "phenotype"). According to their age, the patients were classified as above 65 years (>=65) and below 65 years. Patients with tumor stage I and IA were clustered as stage I, patients with stage II, IIA, IIB as stage II, patients with stage III, IIIA, IIIB, IIIC as stage III, and patients with stage IV, IVA, IVB as stage IV. Patients with microsatellite stability were classified as MSS and patients with microsatellite instability high and low as MSI. The consensus molecular subtypes (CMS) were predicted using the R package CMSClassifier (v1.0.0) and the intrinsic CMS (iCMS) classification of the patients was performed as previously described[56]. The 376 patients affected by CRC were hierarchically clustered according to the high and low expression patterns of the specific gene signatures (Methods Table 3) in the tumor samples. The R packages survival (v3.5.5) and survminer (v0.4.9) were used for survival analysis and plotting the Kaplan-Meier (KM) survival curve. A statistically significant difference in survival was indicated by a log-rank test p-value of $p<0.05$. Survival analysis with univariate and multivariate proportional hazards regression models (Cox regression) was performed to adjust for age, gender, radiation therapy, stage and EGC signature expression. The R packages pheatmap, gtsummary, and ggplot2 were used for visualization.

Methods Table 3

	Gene signature
Enteric glial cells (manually curated from literature[19,25,26])	S100B, SOX10, PLP1, GFAP, CRYAB, CLU, FXYD1, ALDH1A1, PMP22, CDH19, SCN7A, PRNP
$SPP1^+$ TAMs[21]	SPP1, PCSK5, SLC11A1, VCAN, SLC25A37, FLNA, UPP1, BCL6, AQP9, TIMP1, VEGFA, ADM, MARCO, FN1, IL1RN

Gliosis[16]	PTGS2, CD44, CSF1, GCNT2, TGFB1, TUBB6, ICAM1, TNC, TNFRSF12A, RFC3, CP, HMOX1, EPHA4, PVR, PTX3, VCAN, CCL2, CTSB, THBS1, SRXN1, CXCL1, SPHK1, TIMP1, HMGA1, IL6, CXCL2, GFAP, NES, GDNF

Data availability. ScRNA-seq and bulk RNA-seq data generated for this study will be deposited in the Gene Expression Omnibus (GEO) database and will be made publicly available.

Code availability. No custom algorithms were used in the analysis. Code for any specific analysis is available from authors upon request.

REFERENCES

1. Kuipers, E.J., Grady, W.M., Lieberman, D., Seufferlein, T., Sung, J.J., Boelens, P.G., Van De Velde, C.J.H., and Watanabe, T. (2015). Colorectal cancer. Nat. Rev. Dis. Prim. *1*, 1–25. 10.1038/nrdp.2015.65.

2. AlMusawi, S., Ahmed, M., and Nateri, A.S. (2021). Understanding cell-cell communication and signaling in the colorectal cancer microenvironment. Clin. Transl. Med. *11*, e308. 10.1002/ctm2.308.

3. Albo, D., Akay, C.L., Marshall, C.L., Wilks, J.A., Verstovsek, G., Liu, H., Agarwal, N., Berger, D.H., and Ayala, G.E. (2011). Neurogenesis in colorectal cancer is a marker of aggressive tumor behavior and poor outcomes. Cancer *117*, 4834–4845. 10.1002/cncr.26117.

4. Valès, S., Bacola, G., Biraud, M., Touvron, M., Bessard, A., Geraldo, F., Dougherty, K.A., Lashani, S., Bossard, C., Flamant, M., et al. (2019). Tumor cells hijack enteric glia to activate colon cancer stem cells and stimulate tumorigenesis. EBioMedicine *49*, 172–188. 10.1016/j.ebiom.2019.09.045.

5. Yuan, R., Bhattacharya, N., Kenkel, J.A., Shen, J., Dimaio, M.A., Bagchi, S., Prestwood, T.R., Habtezion, A., and Engleman, E.G. (2020). Enteric Glia Play a Critical Role in Promoting the Development of Colorectal Cancer. Front. Oncol. *10*, 1–12. 10.3389/fonc.2020.595892.

6. Neunlist, M., Rolli-Derkinderen, M., Latorre, R., Van Landeghem, L., Coron, E., Derkinderen, P., and De Giorgio, R. (2014). Enteric glial cells: Recent developments and future directions. Gastroenterology *147*, 1230–1237. 10.1053/j.gastro.2014.09.040.

7. Seguella, L., and Gulbransen, B.D. (2021). Enteric glial biology, intercellular signalling and roles in gastrointestinal disease. Nat. Rev. Gastroenterol. Hepatol. *18*, 571–587. 10.1038/s41575-021-00423-7.

8. Thomasi, B., and Gulbransen, B. (2023). Mini-review: Intercellular communication between enteric glia and neurons. Neurosci. Lett. *806*, 137263. 10.1016/j.neulet.2023.137263.

9. Prochera, A., and Rao, M. (2023). Mini-Review: Enteric glial regulation of the gastrointestinal epithelium. Neurosci. Lett. *805*, 137215. 10.1016/j.neulet.2023.137215.

10. Bohórquez, D. V., Samsa, L.A., Roholt, A., Medicetty, S., Chandra, R., and Liddle, R.A. (2014). An enteroendocrine cell - Enteric glia connection revealed by 3D electron microscopy. PLoS One *9*, e89881. 10.1371/journal.pone.0089881.

11. Ibiza, S., García-Cassani, B., Ribeiro, H., Carvalho, T., Almeida, L., Marques, R., Misic, A.M., Bartow-Mckenney, C., Larson, D.M., Pavan, W.J., et al. (2016). Glial-cell-derived neuroregulators control type 3 innate lymphoid cells and gut defence. Nature *535*, 440–443. 10.1038/nature18644.

12. Progatzky, F., Shapiro, M., Chng, S.H., Garcia-Cassani, B., Classon, C.H., Sevgi, S., Laddach, A., Bon-Frauches, A.C., Lasrado, R., Rahim, M., et al. (2021). Regulation of intestinal immunity and tissue repair by enteric glia. Nature *599*, 125–130. 10.1038/s41586-021-04006-z.

13. Grubišić, V., Mcclain, J.L., Fried, D.E., Robson, S.C., Christofi, F.L., and Gulbransen, B.D. (2020). Enteric Glia Modulate Macrophage Phenotype and Visceral Sensitivity following Inflammation. Cell Rep. *32*, 108100. 10.1016/j.celrep.2020.108100.

14. Grubišić, V., Bali, V., Fried, D.E., Eltzschig, H.K., Robson, S.C., Mazei-Robison, M.S., and Gulbransen, B.D. (2022). Enteric glial adenosine 2B receptor signaling mediates persistent epithelial barrier dysfunction following acute DSS colitis. Mucosal Immunol. *15*, 964–976.

10.1038/s41385-022-00550-7.

15. Stakenborg, M., Abdurahiman, S., Simone, V. De, Goverse, G., Stakenborg, N., Baarle, L. Van, Wu, Q., Pirottin, D., Kim, J., Chappell-maor, L., et al. (2022). Enteric glial cells favor accumulation of anti-inflammatory macrophages during the resolution of muscularis in flammation. Mucosal Immunol. *15*, 1296–1308. 10.1038/s41385-022-00563-2.

16. Schneider, R., Leven, P., Mallesh, S., Breßer, M., Schneider, L., Mazzotta, E., Fadda, P., Glowka, T., Vilz, T.O., Lingohr, P., et al. (2022). IL-1-dependent enteric gliosis guides intestinal inflammation and dysmotility and modulates macrophage function. Commun. Biol. *5*, 1–16. 10.1038/s42003-022-03772-4.

17. DeNardo, D.G., and Ruffell, B. (2019). Macrophages as regulators of tumour immunity and immunotherapy. Nat. Rev. Immunol. *19*, 369–382. 10.1038/s41577-019-0127-6.

18. Clarke, L.E., Liddelow, S.A., Chakraborty, C., Münch, A.E., Heiman, M., and Barres, B.A. (2018). Normal aging induces A1-like astrocyte reactivity. Proc. Natl. Acad. Sci. U. S. A. *115*, E1896–E1905. 10.1073/pnas.1800165115.

19. Drokhlyansky, E., Smillie, C.S., Van Wittenberghe, N., Ericsson, M., Griffin, G.K., Eraslan, G., Dionne, D., Cuoco, M.S., Goder-Reiser, M.N., Sharova, T., et al. (2020). The Human and Mouse Enteric Nervous System at Single-Cell Resolution. Cell *182*, 1606–1622. 10.1016/j.cell.2020.08.003.

20. Baghdadi, M.B., Ayyaz, A., Coquenlorge, S., Streutker, C., Wrana, J.L., Kim, T., Baghdadi, M.B., Ayyaz, A., Coquenlorge, S., Chu, B., et al. (2021). Enteric glial cell heterogeneity regulates intestinal stem cell niches. Cell Stem Cell *29*, 1–15. 10.1016/j.stem.2021.10.004.

21. Zhang, L., Li, Z., Skrzypczynska, K.M., Fang, Q., Zhang, W., O'Brien, S.A., He, Y., Wang, L., Zhang, Q., Kim, A., et al. (2020). Single-Cell Analyses Inform Mechanisms of Myeloid-Targeted Therapies in Colon Cancer. Cell *181*, 442–459. 10.1016/j.cell.2020.03.048.

22. Browaeys, R., Saelens, W., and Saeys, Y. (2020). NicheNet: modeling intercellular communication by linking ligands to target genes. Nat. Methods *17*, 159–162. 10.1038/s41592-019-0667-5.

23. Schneider, R., Leven, P., Glowka, T., Kuzmanov, I., Lysson, M., Schneiker, B., Miesen, A., Baqi, Y., Spanier, C., Grants, I., et al. (2021). A novel P2X2-dependent purinergic mechanism of enteric gliosis in intestinal inflammation. EMBO Mol. Med. *13*, 1–20. 10.15252/emmm.202012724.

24. Afik, R., Zigmond, E., Vugman, M., Klepfish, M., Shimshoni, E., Pasmanik-Chor, M., Shenoy, A., Bassat, E., Halpern, Z., Geiger, T., et al. (2016). Tumor macrophages are pivotal constructors of tumor collagenous matrix. J. Exp. Med. *213*, 2315–2331. 10.1084/jem.20151193.

25. Lee, H.O., Hong, Y., Etlioglu, H.E., Cho, Y.B., Pomella, V., Van den Bosch, B., Vanhecke, J., Verbandt, S., Hong, H., Min, J.W., et al. (2020). Lineage-dependent gene expression programs influence the immune landscape of colorectal cancer. Nat. Genet. *52*, 594–603. 10.1038/s41588-020-0636-z.

26. Kinchen, J., Chen, H.H., Parikh, K., Antanaviciute, A., Jagielowicz, M., Fawkner-Corbett, D., Ashley, N., Cubitt, L., Mellado-Gomez, E., Attar, M., et al. (2018). Structural Remodeling of the Human Colonic Mesenchyme in Inflammatory Bowel Disease. Cell *175*, 372–386. 10.1016/j.cell.2018.08.067.

27. Guinney, J., Dienstmann, R., Wang, X., De Reyniès, A., Schlicker, A., Soneson, C., Marisa, L., Roepman, P., Nyamundanda, G., Angelino, P., et al. (2015). The consensus molecular subtypes

of colorectal cancer. Nat. Med. *21*, 1350–1356. 10.1038/nm.3967.

28. Stoffels, B., Hupa, K.J., Snoek, S.A., Van Bree, S., Stein, K., Schwandt, T., Vilz, T.O., Lysson, M., Veer, C.V.T., Kummer, M.P., et al. (2014). Postoperative ileus involves interleukin-1 receptor signaling in enteric glia. Gastroenterology *146*, 176–187. 10.1053/j.gastro.2013.09.030.

29. Qi, J., Sun, H., Zhang, Y., Wang, Z., Xun, Z., Li, Z., Ding, X., Bao, R., Hong, L., Jia, W., et al. (2022). Single-cell and spatial analysis reveal interaction of FAP+ fibroblasts and SPP1+ macrophages in colorectal cancer. Nat. Commun. *13*, 1742. 10.1038/s41467-022-29366-6.

30. Luo, H., Xia, X., Huang, L.-B., An, H., Cao, M., Kim, G.D., Chen, H.-N., Zhang, W.-H., Shu, Y., Kong, X., et al. (2022). Pan-cancer single-cell analysis reveals the heterogeneity and plasticity of cancer- associated fi broblasts in the tumor microenvironment. Nat. Commun. *13*, 6619. 10.1038/s41467-022-34395-2.

31. Cheng, S., Li, Z., Gao, R., Xing, B., Gao, Y., Yang, Y., Qin, S., Zhang, L., Ouyang, H., Du, P., et al. (2021). A pan-cancer single-cell transcriptional atlas of tumor infiltrating myeloid cells. Cell *184*, 792–809. 10.1016/j.cell.2021.01.010.

32. Pundavela, J., Roselli, S., Faulkner, S., Attia, J., Scott, R.J., Thorne, R.F., Forbes, J.F., Bradshaw, R.A., Walker, M.M., Jobling, P., et al. (2015). Nerve fibers infiltrate the tumor microenvironment and are associated with nerve growth factor production and lymph node invasion in breast cancer. Mol. Oncol. *9*, 1626–1635. 10.1016/j.molonc.2015.05.001.

33. Renz, B.W., Takahashi, R., Tanaka, T., Macchini, M., Hayakawa, Y., Dantes, Z., Maurer, H.C., Chen, X., Jiang, Z., Westphalen, C.B., et al. (2018). β2 Adrenergic-Neurotrophin Feedforward Loop Promotes Pancreatic Cancer. Cancer Cell *33*, 75–90. 10.1016/j.ccell.2017.11.007.

34. Hayakawa, Y., Sakitani, K., Konishi, M., Asfaha, S., Niikura, R., Tomita, H., Renz, B.W., Tailor, Y., Macchini, M., Middelhoff, M., et al. (2017). Nerve Growth Factor Promotes Gastric Tumorigenesis through Aberrant Cholinergic Signaling. Cancer Cell *31*, 21–34. 10.1016/j.ccell.2016.11.005.

35. Albergotti, W.G., Schwarzbach, H.L., Abberbock, S., Ferris, R.L., Johnson, J.T., Duvvuri, U., and Kim, S. (2017). Defining the prevalence and prognostic value of perineural invasion and angiolymphatic invasion in human papillomavirus-positive oropharyngeal carcinoma. JAMA Otolaryngol. - Head Neck Surg. *143*, 1236–1243. 10.1001/jamaoto.2017.2019.

36. Zhu, Y., Zhang, G., Yang, Y., Cui, L., Jia, S., Shi, Y., Song, S., and Xu, S. (2018). Perineural invasion in early-stage cervical cancer and its relevance following surgery. Oncol. Lett. *15*, 6555–6561. 10.3892/ol.2018.8116.

37. Murakami, Y., Uemura, K., Sudo, T., Hashimoto, Y., Kondo, N., Nakagawa, N., Muto, T., Sasaki, H., Urabe, K., and Sueda, T. (2013). Perineural Invasion in Extrahepatic Cholangiocarcinoma: Prognostic Impact and Treatment Strategies. J. Gastrointest. Surg. *17*, 1429–1439. 10.1007/s11605-013-2251-0.

38. Magnon, C., Hall, S., Lin, J., Xue, X., Gerber, L., Freedland, S., and Frenette, P. (2013). Autonomic Nerve Development Contributes to Prostate Cancer Progression. Science. *341*, 1236361. 10.1038/aja.2013.113.

39. Deborde, S., Gusain, L., Powers, A., Marcadis, A., Yu, Y., Chen, C.H., Frants, A., Kao, E., Tang, L.H., Vakiani, E., et al. (2022). Reprogrammed Schwann Cells Organize into Dynamic Tracks that Promote Pancreatic Cancer Invasion. Cancer Discov. *12*, 2454–2473. 10.1158/2159-8290.CD-21-1690.

40. Zhou, Y., Li, J., Han, B., Zhong, R., and Zhong, H. (2020). Schwann cells promote lung cancer

proliferation by promoting the M2 polarization of macrophages. Cell. Immunol. *357*, 104211. 10.1016/j.cellimm.2020.104211.

41. Shurin, G. V., Kruglov, O., Ding, F., Lin, Y., Hao, X., Keskinov, A.A., You, Z., Lokshin, A.E., LaFramboise, W.A., Falo, L.D., et al. (2019). Melanoma-induced reprogramming of schwann cell signaling aids tumor growth. Cancer Res. *79*, 2736–2747. 10.1158/0008-5472.CAN-18-3872.

42. Zhang, P., Gu, Y., Fang, H., Cao, Y., Wang, J., Liu, H., Zhang, H., Li, H., He, H., Li, R., et al. (2022). Intratumoral IL-1R1 expression delineates a distinctive molecular subset with therapeutic resistance in patients with gastric cancer. J. Immunother. Cancer *10*, e004047. 10.1136/jitc-2021-004047.

43. Zigmond, E., Halpern, Z., Elinav, E., Brazowski, E., Jung, S., and Varol, C. (2011). Utilization of murine colonoscopy for orthotopic implantation of colorectal cancer. PLoS One *6*, 1–7. 10.1371/journal.pone.0028858.

44. Parang, B., Barrett, C.W., and Williams, C.S. (2016). AOM/DSS Model of Colitis-Associated Cancer. In Methods Mol Biol, pp. 297–307. 10.3109/00365521.2015.1009157.

45. Pombo Antunes, A.R., Scheyltjens, I., Lodi, F., Messiaen, J., Antoranz, A., Duerinck, J., Kancheva, D., Martens, L., De Vlaminck, K., Van Hove, H., et al. (2021). Single-cell profiling of myeloid cells in glioblastoma across species and disease stage reveals macrophage competition and specialization. Nat. Neurosci. *24*, 595–610. 10.1038/s41593-020-00789-y.

46. Maria Bosisio, F., Antoranz, A., Van Herck, Y., Maria Bolognesi, M., Marcelis, L., Chinello, C., Wouters, J., Magni, F., Alexopoulos, L., Stas, M., et al. (2020). Functional heterogeneity of lymphocytic patterns in primary melanoma dissected through single-cell multiplexing. Elife *9*, 1–28. 10.7554/eLife.53008.

47. Naulaerts, S., Datsi, A., Borras, D.M., Antoranz Martinez, A., Messiaen, J., Vanmeerbeek, I., Sprooten, J., Laureano, R.S., Govaerts, J., Panovska, D., et al. (2023). Multiomics and spatial mapping characterizes human CD8+ T cell states in cancer. Sci. Transl. Med. *15*, eadd1016. 10.1126/scitranslmed.add1016.

48. Mellacheruvu, D., Wright, Z., Couzens, A.L., Lambert, J.P., St-Denis, N.A., Li, T., Miteva, Y. V., Hauri, S., Sardiu, M.E., Low, T.Y., et al. (2013). The CRAPome: A contaminant repository for affinity purification-mass spectrometry data. Nat. Methods *10*, 730–736. 10.1038/nmeth.2557.

49. The, M., MacCoss, M.J., Noble, W.S., and Käll, L. (2016). Fast and Accurate Protein False Discovery Rates on Large-Scale Proteomics Data Sets with Percolator 3.0. J. Am. Soc. Mass Spectrom. *27*, 1719–1727. 10.1007/s13361-016-1460-7.

50. Ritchie, M.E., Phipson, B., Wu, D., Hu, Y., Law, C.W., Shi, W., and Smyth, G.K. (2015). Limma powers differential expression analyses for RNA-sequencing and microarray studies. Nucleic Acids Res. *43*, e47. 10.1093/nar/gkv007.

51. Kim, D., Paggi, J.M., Park, C., Bennett, C., and Salzberg, S.L. (2019). Graph-based genome alignment and genotyping with HISAT2 and HISAT-genotype. Nat. Biotechnol. *37*, 907–915. 10.1038/s41587-019-0201-4.

52. Li, H., Handsaker, B., Wysoker, A., Fennell, T., Ruan, J., Homer, N., Marth, G., Abecasis, G., and Durbin, R. (2009). The Sequence Alignment/Map format and SAMtools. Bioinformatics *25*, 2078–2079. 10.1093/bioinformatics/btp352.

53. Anders, S., Pyl, P.T., and Huber, W. (2015). HTSeq-A Python framework to work with high-

throughput sequencing data. Bioinformatics *31*, 166–169. 10.1093/bioinformatics/btu638.

54. Love, M.I., Huber, W., and Anders, S. (2014). Moderated estimation of fold change and dispersion for RNA-seq data with DESeq2. Genome Biol. *15*, 1–21. 10.1186/s13059-014-0550-8.

55. Langfelder, P., and Horvath, S. (2008). WGCNA: An R package for weighted correlation network analysis. BMC Bioinformatics *9*, 1–13. 10.1186/1471-2105-9-559/FIGURES/4.

56. Joanito, I., Wirapati, P., Zhao, N., Nawaz, Z., Yeo, G., Lee, F., Eng, C.L.P., Macalinao, D.C., Kahraman, M., Srinivasan, H., et al. (2022). Single-cell and bulk transcriptome sequencing identifies two epithelial tumor cell states and refines the consensus molecular classification of colorectal cancer. Nat. Genet. *54*, 963–975. 10.1038/s41588-022-01100-4.